Supplementary Information (SI) for EES Solar.
This journal is © The Royal Society of Chemistry 2026

Supporting Information

HTL- & ETL-free Metal-Semiconductor-Metal Structure Organic Solar Cells

Sujung Park,‡[a] Hong Nhan Tran,‡[a] , Heunjeong Lee,‡[a] Seul Lee,[b] Young Wan Lee,[b] Jin Hee Lee,[c] Jina Roe,[d] Muhammad Jahandar,[e] Nurul Kusuma Wardani,[ei] Jin Young Kim,[df] Jung Hwa Seo,[c] Hoe-Yeon Jeong,[g] Eun-chae Jeon,[g] Young S. Park,[b] Soyeon Kim,[e] Bong Soo Kim,*[bfh] Dong Chan Lim*[e] and Shinuk Cho*[a]

[a]Department of Semiconductor Physics & Engineering and Energy Harvest Storage Research Center, University of Ulsan, Ulsan 44610, Republic of Korea. E-mail: sucho@ulsan.ac.kr

[b]Department of Chemistry, Ulsan National Institute of Science and Technology (UNIST), Ulsan 44919, Republic of Korea. E-mail: bongsoo@unist.ac.kr

[c]Department of Physics, University of Seoul, Seoul 02504, Republic of Korea

[d]Department of Energy Engineering and School of Energy and Chemical Engineering, UNIST, Ulsan 44919, Republic of Korea

[e]Energy & Environment Materials Research Division, Surface Materials Division, Korea Institute of Materials Science (KIMS), Changwon 51508, Republic of Korea. E-mail: dclim@kims.re.kr

[f]Graduate School of Carbon Neutrality, UNIST, Ulsan 44919, Republic of Korea.

[g]School of Materials Science and Engineering, University of Ulsan, Ulsan 44776, Republic of Korea

[h]Graduate School of Semiconductor Materials and Device Engineering, UNIST, Ulsan 44919, Republic of Korea

[i]Department of Smart Green Technology Engineering, Pukyong National University, Busan 48513, Republic of Korea

‡ S. Park, H. N. Tran and H. Lee contributed equally to this work.

Materials

The polymer donors PM6 and PTB7-Th, and non-fullerene acceptors IEICO-4F, Y6 and L8-BO were purchased from 1-materials. Br-2EPSe and PDINN were provided by B.S. Kim's group (UNIST). PEDOT:PSS (Clevios P VP AI4083) was purchased from Heraeus. THA-I, Rb-TPB and PTA, and all solvents were purchased from Sigma-Aldrich.

Device fabrication

In all MSM-type devices, the ITO substrates were cleaned with acetone and isopropyl alcohol in an ultrasonic bath for 15 min each and dried at 110 ℃ for 2 h in the oven before use.

MSM type-I device: The MSM type-I device was fabricated with the structure ITO/Br-2EPSe/PM6:L8-BO/THA-I/Ag. After UV-ozone surface treatment, a Br-2EPSe solution (1 mM in ethanol) was spin-coated onto the ITO substrates at 4000 rpm for 30 s and subsequently annealed at 100 ℃ for 10 min in air. The ITO substrates were then transferred to a N_2-filled glove box for further processing. The PM6:L8-BO solution for the photoactive layer was prepared at a total concentration of 17.6 mg/ml with a donor-to-acceptor (D:A) ratio of 1:1.2 in chloroform, containing 0.7% 1-fluoronaphthalene as an additive. The solution was stirred for 3 hours prior to use. This PM6:L8-BO solution was spin-coated onto the Br-2EPSe layer at 4000 rpm for 30 s and annealed at 100 ℃ for 10 min. Next, a layer of PDINN (1 mg/ml in methanol) or THA-I (0.2 mg/ml in isopropyl alcohol) was spin-coated onto the photoactive layer at 5000 rpm for 30 s. Finally, a 100-nm-thick Ag electrode was thermally evaporated under vacuum at a pressure of 2×10^{-6} torr through a shadow mask. The active area of the device was 0.0319 cm^2

MSM type-II device: The MSM-type II device was fabricated with the structure ITO/Rb-TPB/PTB7-Th:IEICO-4F/THA-I/Ag. All fabrication steps were conducted inside a N_2-filled glove box. The Rb-TPB, diluted in chlorobenzene, was spin-coated onto the ITO substrate at 5000 rpm for 30 s. The PTB7-Th:IEICO-4F solution for the photoactive layer was prepared at a total concentration of 20.0 mg/ml with a donor-to-acceptor (D:A) ratio of 1:1.5 in chlorobenzene, containing 4% 1-chloronaphthalene (CN) as an additive. The solution was stirred for 1 day prior to use. The PTB7-Th:IEICO-4F solution was spin-coated at 1400 rpm, followed by a second spin at 9000 rpm to remove residual CN. The THA-I solution was subsequently spin-coated onto the photoactive layer at 5000 rpm for 30 s without requiring annealing. Finally, a 100-nm-thick Ag electrode was thermally evaporated under vacuum at a pressure of 2×10^{-6} torr using a shadow mask. The active area of the device was 0.13 cm^2.

MSM type-III device: The MSM type-III device was fabricated with the structure ITO/PM6:Y6+PTA/THA-I/Ag. All fabrication steps were conducted inside a N_2-filled glove box. The PM6:Y6 solution for the photoactive layer was prepared at a total concentration of

17.6 mg/ml with a donor-to-acceptor (D:A) ratio of 1:1.2 in chloroform, containing 0.5% CN as an additive. PTA was dissolved in methanol at a concentration of 1.5 mg/ml and added to the PM6:Y6 solution at 5% by volume. The PM6:Y6+PTA mixed solution was stirred for 3 hours prior to use. This solution was then spin-coated onto the ITO substrate at 5000 rpm for 30 s. Subsequently, the THA-I layer was spin-coated on top of the photoactive layer at 5000 rpm for 30 s. Finally, a 100-nm-thick Ag electrode was thermally evaporated under vacuum at a pressure of 2×10^{-6} torr using a shadow mask. The active area of the device was 0.0319 cm^2.

Scale-Up Module Device: The large-area ITO substrates (10×10 cm^2) were used as received from the supplier without any solvent cleaning. The substrates were treated with UV ozone for 15 min. The preparation conditions for the PM6:Y6+PTA and THA-I solutions were identical to those used for the Type-III devices. Subsequently, the photoactive layer solution was printed onto the large-area ITO substrate using a metal pattern mask, enabling direct patterning of the module layout. Subsequently, a 100 nm thick Ag electrode was thermally evaporated under high vacuum at a pressure of 10^{-7} torr using a shadow mask. The active area of the module device was 54 cm^2.

Measurements and instruments

Characterization and performance measurement of OSCs

The power conversion efficiencies of the organic solar cells were measured by *J-V* curves using a Keithley 2401 sourcemeter under AM 1.5G 100 mW/cm^2 spectra from a solar simulator (McScience Inc., K201 LAB55 and SimuLight PLS300). To calibrate the intensity of the solar simulator, a standard Si-photodiode detector with a KG-3 filter (Newport Co., Oriel) was used. The EQE was measured using a quantum efficiency measurement system solar cell spectral response/QE/IPCE (Newport Co., Oriel IQE-200B). The light intensity at each wavelength was calibrated using a standard, single-crystal Si photovoltaic cell. The J_{SC}s were consistent with the EQE J_{SC}s within 5% error. The surface properties of the PM6:L8-BO layers were characterized by NanoNavi II AFM system (SII Nano Technology Inc.) in tapping mode. The potential distribution of ITO with Rb-TPB and, PM6:L8-BO with THA-I were measured by KPFM. Non-modulated impedance spectroscopy, IMVS and IMPS were performed using an impedance analyzer (IVIUM Tech., IviumStat) at an open circuit voltage with a small perturbation in the frequency range between 0.1 Hz and 1.0 MHz under dark. TPC and TPV measurements were conducted using the analyzer function of an organic semiconductor parameter test system (McScience Inc., T4000) at V_{OC} conditions under 1 sun illumination. UPS and XPS were performed using a Thermofisher Nexsa surface analysis system equipped with a He-discharge lamp, proving He-I photons with an energy of 21.22 eV for UPS analysis, and a monochromatic Al-Ka X-ray gun with photon energies of 1486.6 eV for XPS investigation. The base vacuum pressure of the analysis system was ~10^{-7} torr. The Fermi edge was calibrated using a thermally evaporated Au film, and all spectra presented were plotted relative to this reference E_F. WFs were obtained from the difference between the

incident photon energy (21.22 eV) and the secondary edge (E_{SE}) as follows: WF = 21.22 eV - E_{SE}.

Light intensity dependence of OSCs parameter

The *J-V* characteristics under various illumination conditions were measured using a Keithley 2401 source measurement unit connected to a solar simulator (Newport Co., Oriel). The solar simulator was operated at 1 sun (100 mW/cm^2) and equipped with a set of neutral density filters to adjust the light intensities, enabling the investigation of J_{SC} and V_{OC} dependencies. A standard Si photodiode detector with a KG-3 filter (Newport Co., Oriel) was used to calibrate the light intensity.

The linear dependence of J_{SC} on the light intensity can be expressed as a power law,[1]

$(I \propto {J_{SC}}^{\alpha})$

The straight line in the semilogarithmic plot of V_{OC} versus light intensity can be described using the expression:

$$V_{OC} = \frac{nk_BT}{q} ln\left(\frac{I}{I_0}\right)$$

where q is the elementary charge, n is the ideality factor, k_B is the Boltzmann constant, T is the temperature, I is the light intensity, and I_0 is the initial light intensity.[2]

Impedance spectroscopy (IS) and capacitance-voltage (C-V) measurements

The non-modulated IS, IMVS, IMPS, and C-V measurements were performed using an impedance analyzer (IVIUM Tech., IviumStat). The impedance spectrum was recorded at the open-circuit voltage with a small perturbation applied across a frequency range of 0.1 Hz to 1 MHz under dark conditions. The C-V measurements were conducted at a frequency of 1 kHz to extract V_{bi}.

Space charge limited current (SCLC) measurements

Single-carrier devices were fabricated with the structure ITO/ZnO/PM6:L8-BO/ETL/Ag. The dark *J-V* characteristics were measured and analyzed in the SCLC regime. Assuming field-independent mobility, the electron mobility can be described using the Mott-Gurney equation as follows:

$$J = 9\epsilon_0\epsilon_r\mu V^2/8L^3$$

where ϵ_0 is permittivity of free space (8.85x10^{-12} F/m), ϵ_r is the dielectric constant of

photoactive layer, μ_e is electron mobility, V is the voltage drop across the device, L is the thickness of photoactive layer.[3,4] In this mobility calculation, ϵ_r was determined by the capacitance value at a 1 kHz frequency and V=0 V in dark conditions, according to $C=\epsilon_0\epsilon_r A/L$, yielding a value of 5.3.[5] L was taken as the measured thickness of 147 nm from layer thickness measurements (Fig. S4).

Photocurrent density (J_{ph})-effective voltage (V_{eff}) measurements

The dependence of J_{ph} on V_{eff} on a logarithmic scale was measured both in the dark and under 1-sun illumination. Here, $J_{ph}= J_L-J_D$, where J_L is the current density under illumination, and J_D is the current density in the dark. Additionally, $V_{eff}=V_0-V_a$, where V_0 is the compensation voltage at $J_{ph}=0$, and V_a is the applied voltage.[6] The saturation photocurrent density (J_{sat}) can be obtained from the region of the photocurrent density curve where saturation occurs. This saturation is determined by the absorbed incident photon flux and is independent of both bias and temperature. The exciton generation rate (G_{max}) can be calculated using the following equation, assuming all photogenerated excitons dissociate and contribute to the current in the saturated region due to a sufficiently high electric field:

$$J_{sat}=qG_{max}L$$

where q is the elementary charge, and L is the thickness of the photoactive layer.[7] The exciton dissociation efficiency (η_{diss}) can be expressed as $\eta_{diss}=J_{ph}/J_{sat}$ under short-circuit conditions. The charge collection efficiency (η_{coll}) can be expressed as $\eta_{coll}=J_{ph}/J_{sat}$ under maximum power output conditions.[8,9]

Kevin probe force microscopy (KPFM) measurements

The contact potential difference (CPD) of each film was measured using an Rb-coated Si cantilever tip with a 1 V bias. When a CPD is formed between the biased tip and the sample, an electric field induces the movement of electrons to align the Fermi levels of the two.[10] This movement direction is reflected as positive or negative CPD values. A change in the CPD value in the positive (negative) direction indicates a lower (higher) Fermi level relative to the reference sample. The potential distribution was obtained by extracting line profiles from the potential data measured using KPFM.

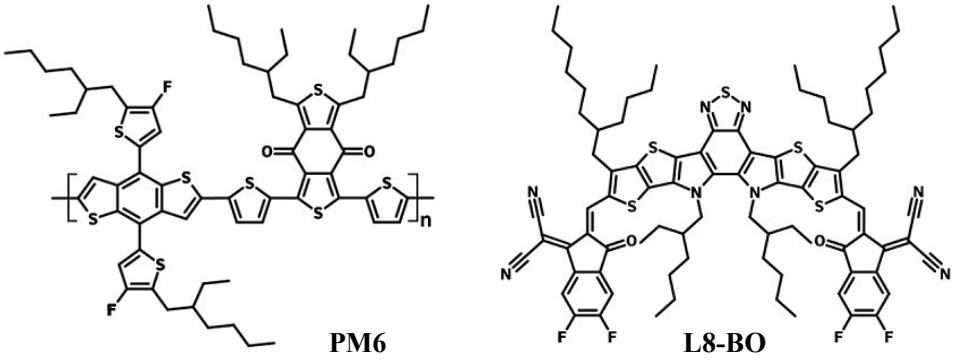

Figure S1. Chemical structures. The chemical structures of the materials used in MSM type-I devices: the donor PM6 and the non-fullerene acceptor L8-BO.

MSM type-I devices incorporating tetra-alkyl-iodide salts with different alkyl chain lengths

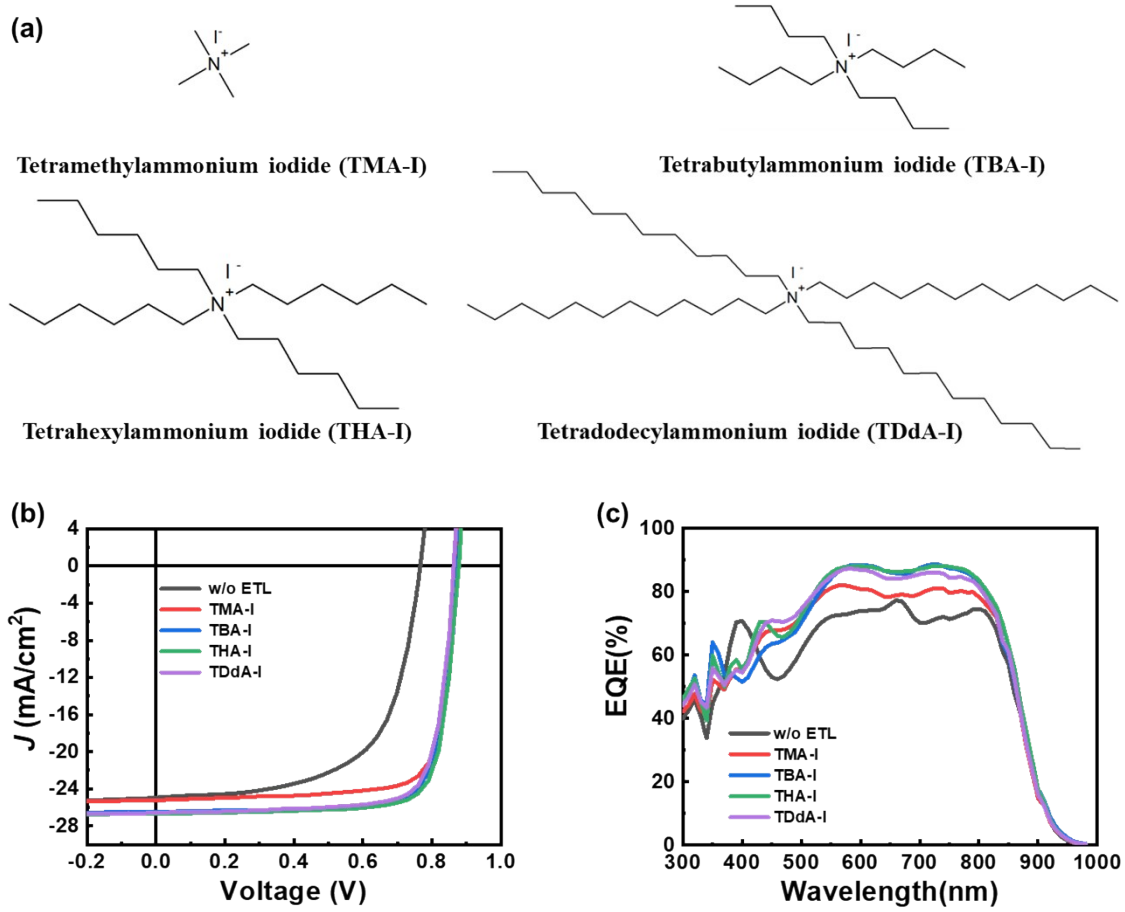

Figure S2. (a) Chemical structure of tetra-alkyl-iodide salts with varying alkyl chain lengths, (b) *J-V* characteristics of MSM type-I devices incorporating tetra-alkyl-iodide salts with different alkyl chain lengths, and (c) the corresponding EQE spectra.

Table S1. Photovoltaic performance parameters of MSM type-I devices incorporating tetra-alkyl-iodide salts with varying alkyl chain lengths.

Tetra-Alkyl-Ammonium Iodide	V_{OC} [V]	J_{SC} [mA/cm²]	FF [%]	PCE [%]	PCE_{Avg} [%]
None	0.766	24.865	62.51	11.93	10.69±0.70
TMA-I	0.872	25.209	78.22	17.17	16.64±0.32
TBA-I	0.875	26.213	78.54	18.01	17.62±0.27
THA-I	0.877	26.695	78.68	18.41	18.05±0.23
TDda-I	0.865	26.568	78.17	17.96	17.54±0.29

MSM type-I devices as a function of the counter ion variation in tetra-butyl-based salts

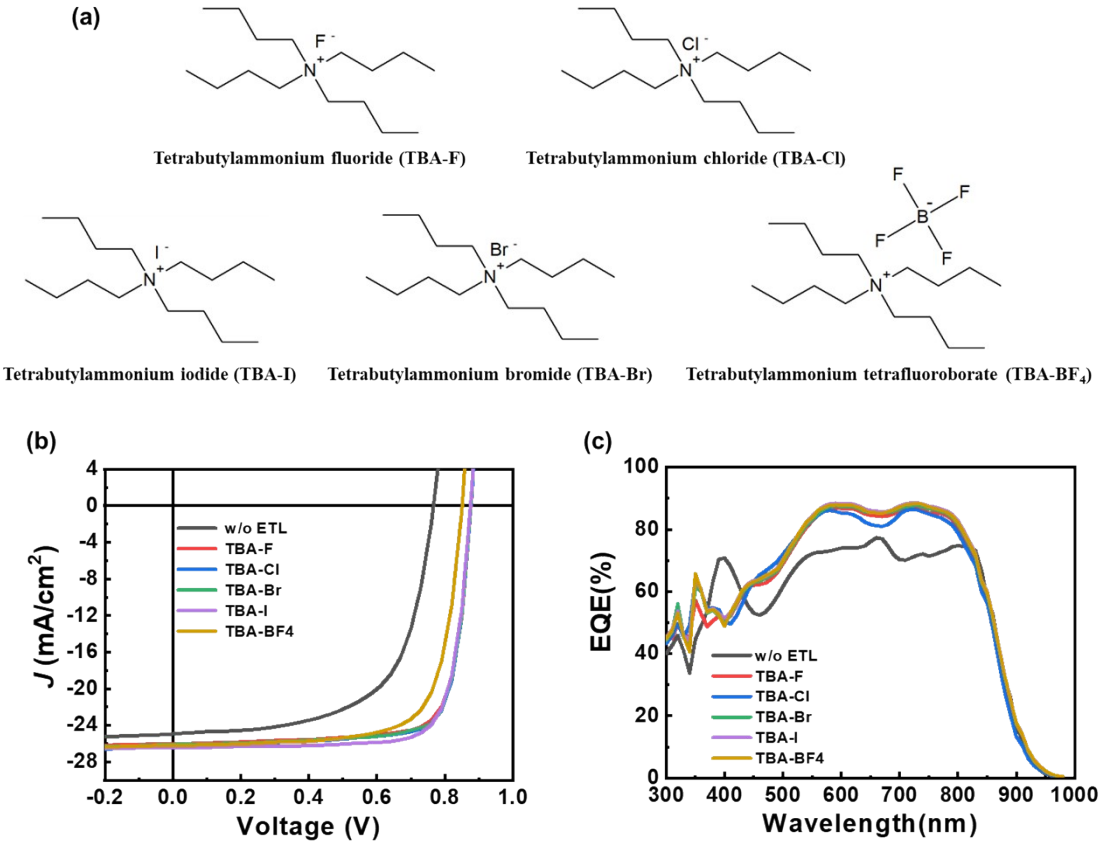

Figure S3. (a) Chemical structures of tetra-butyl-based salts with different counter ions, (b) *J-V* characteristics of MSM type-I devices as a function of the counter ion variation in tetra-butyl-based salts, and (c) the corresponding EQE spectra.

Table S2. Photovoltaic performance parameters of MSM type-I devices depending on the counter ion variation in tetra-butyl-based salts.

TBA-X, (X=F, Cl, Br, I, BF_4)	**V_{OC} [V]**	**J_{SC} [mA/cm²]**	**FF**	**PCE [%]**	**PCE_{Avg} [%]**
w/o ETL	0.766	24.865	62.51	11.93	10.69±0.70
TBA-F	0.877	25.764	78.14	17.65	17.28±0.30
TBA-Cl	0.876	26.048	78.38	17.88	17.46±0.31
TBA-Br	0.875	26.083	78.49	17.91	17.52±0.28
TBA-I	0.875	26.209	78.54	18.01	17.62±0.27
TBA-BF_4	0.851	26.192	73.25	16.32	15.94±0.31

Film thickness measurements

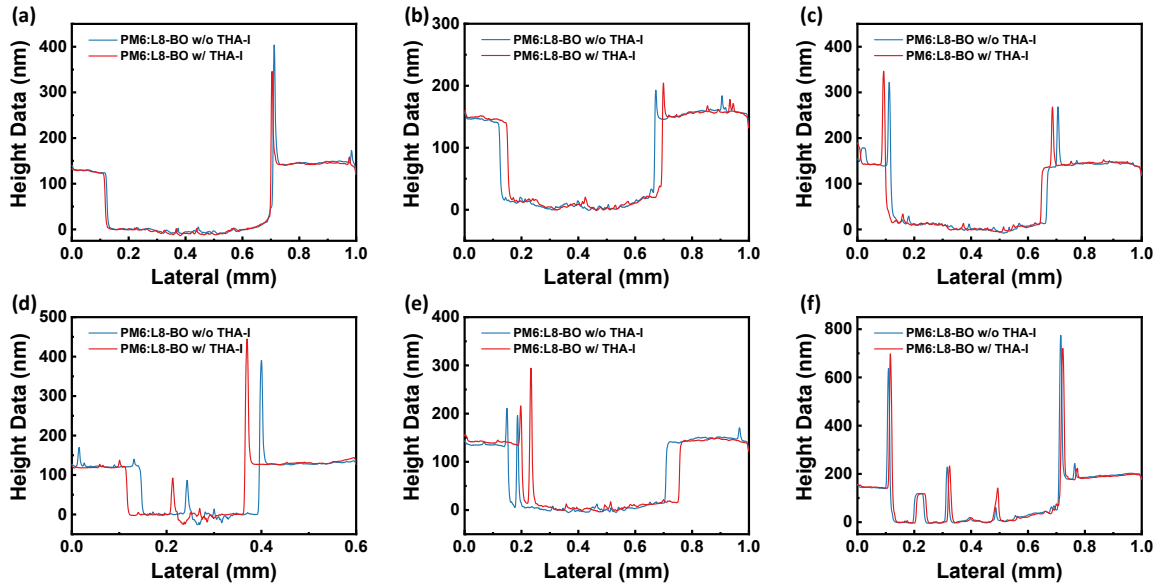

Figure S4. Surface profile of film thickness measurements.

Table S3. Device structures of the samples prepared and analyzed for XPS measurements in this study. All samples were prepared on bare silicon substrates.

Notation	Device structure
Ag	Si/Ag [ca. 70 nm]
THA-I	Si/THA-I
Ag/THA-I	Si/Ag [ca. 70 nm]/THA-I
BHJ (PM6:L8-BO)	Si/Ag [ca. 70 nm]/photoactive layer [ca. 120 nm]
BHJ/THA-I	Si/Ag [ca. 70 nm]/photoactive layer [ca. 120 nm]/THA-I
BHJ/THA-I/Ag	Si/Ag [ca. 70 nm]/photoactive layer [ca. 120 nm]/THA-I/Ag [ca. 1 nm]

Mott-Schottky analysis

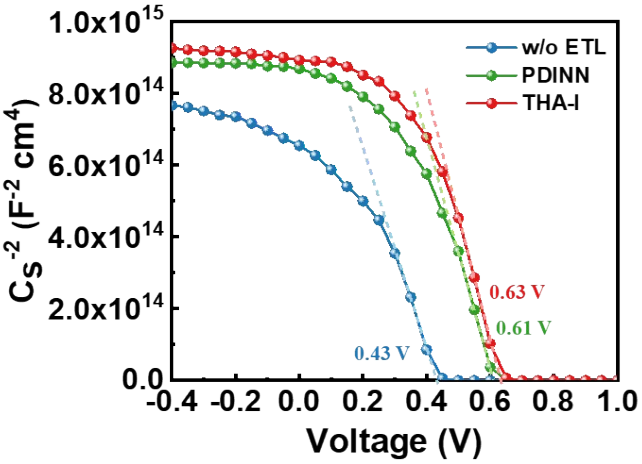

Figure S5. Mott-Schottky plot of the C-V response for MSM type-I devices measured at 1 kHz.

To directly confirm the change in V_{bi} caused by the interfacial dipole induced by THA-I treatment, Mott-Schottky analysis was performed. The linear region of the Mott-Schottky plot, where it intersects the x-axis, represents V_{bi}.[11] After THA-I treatment, V_{bi} increased from 0.43 to 0.63 V, which is higher than the value observed when PDINN is used as the ETL. Considering that THA-I processing is the primary difference in devices without an ETL, it is evident that the dipole effect of THA-I strengthens V_{bi}.

Table S4. Exciton generation rate (G_{max}), exciton dissociation probability (η_{diss}) and charge collection efficiency (η_{coll}) of the MSM type-I device calculated from J_{ph}-V_{eff} measurements.

Device	G_{max} ($m^{-3}s^{-1}$)	η_{diss} (%)	η_{coll} (%)
w/o ETL	1.33×10^{28}	82.7	76.7
PDINN	3.24×10^{28}	96.1	90.4
THA-I	3.67×10^{28}	96.3	91.5

Light intensity dependence of J_{SC} and V_{OC}

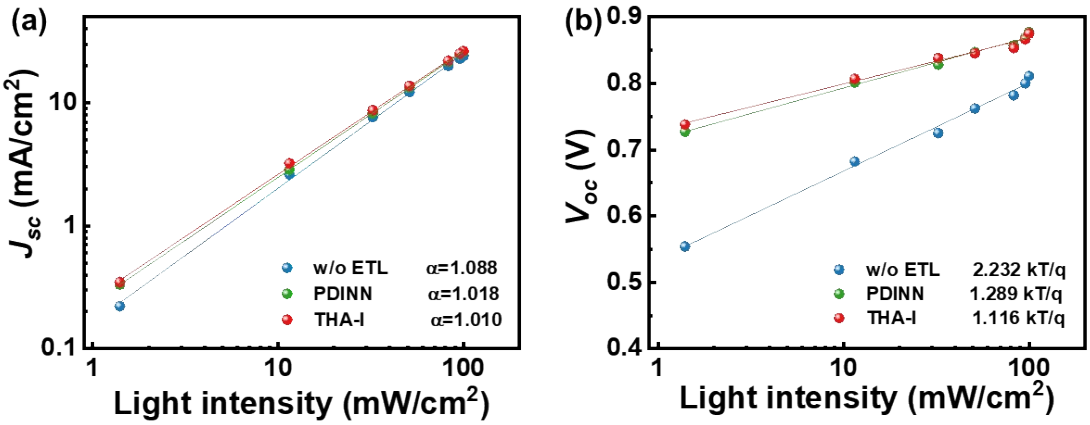

Figure S6. Charge carrier recombination and lifetime analysis. Light intensity dependence of (a) J_{SC} and (b) V_{OC} characteristics in MSM type-I device.

To gain insights into the charge recombination mechanisms within MSM type-I devices, the dependence of J_{SC} and V_{OC} on light intensity, ranging from 1.25 to 100 mW/cm^2, was analyzed. Information on charge recombination can be obtained from the slope of the relationship between J_{SC} and light intensity. A slope (α) close to 1 indicates weak bimolecular recombination.[12]

The device without an ETL showed a slope of 1.088, whereas the device with THA-I treatment exhibited a significantly lower slope of 1.010 in the J_{SC}-light intensity characteristic (Fig. S6a). These results suggest that introducing THA-I treatment suppresses bimolecular recombination, consistent with the observed increase in J_{SC} for THA-I-treated devices.[13]

For V_{OC}-light intensity characteristics, a slope close to kT/q indicates that bimolecular recombination is dominant. If the slope approaches 2 kT/q, it suggests that trap-assisted recombination is the primary process in the device. As shown in Fig. S6b, the slope for the device without an ETL was calculated to be 2.232 kT/q, while the slope for the device with THA-I treatment was 1.116 kT/q. The reduced slope in the THA-I-treated device indicates that trap-assisted recombination was suppressed.[14,15]

SCLC Measurements

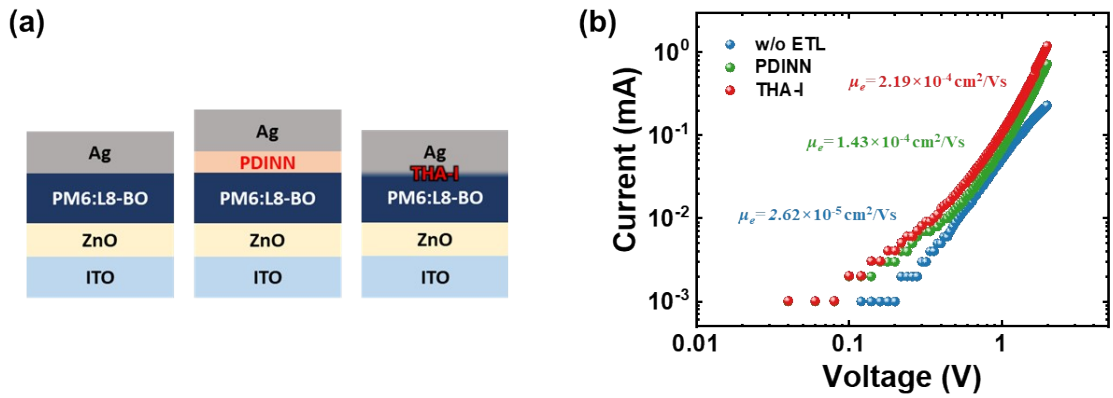

Figure S7. Electrical measurements of the electron transport characteristics in MSM type-I devices. (a) Schematic device architecture of the electron-only device for space charge limited current (SCLC) measurements, and (b) log(J)-log(V) plots for electron-only devices.

To investigate charge mobility and charge transport properties, the SCLC technique was used to calculate the electron mobility (μ_e). The dark J-V curves measured from electron-only devices without an ETL, with a PDINN layer, and with THA-I treatment are shown in Fig. S7b. The μ_e of the device without an ETL is 2.62×10^{-5} cm^2/Vs, which increases to 2.19×10^{-4} cm^2/Vs with THA-I treatment, indicating that charge transport is enhanced by THA-I. This trend is also observed in the mobility calculated through organic thin-film transistor measurements (Fig. S10).

Impedance spectroscopy (IS)

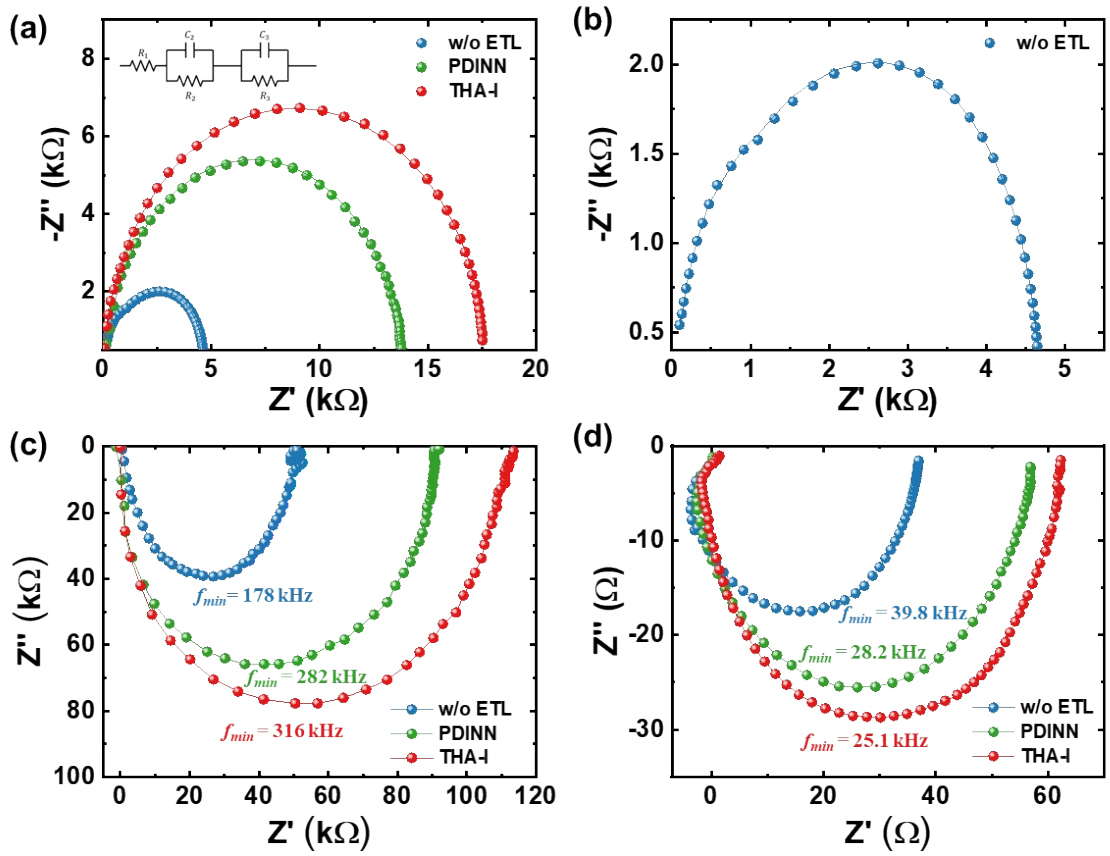

Figure S8. (a) Non-modulated impedance spectroscopy (IS) under dark conditions, (b) a magnified view of the non-modulated impedance spectroscopy for the device without an ETL, (c) IMPS, and (d) IMVS of the MSM type-I device.

IS was performed at V_{OC} under dark conditions, and the data were fitted to equivalent circuits. The Nyquist plots of non-modulated IS are shown in Fig. S8a. The diameter of the semicircle represents the charge recombination resistance (R_{rec}), where a larger R_{rec} typically indicates delayed charge recombination, implying efficient carrier transport.[16, 17] The device without any ETL shows a very small semicircle, indicating a lower R_{rec}. Upon closer inspection, the semicircle appears to split into two (Fig. S8b), suggesting significant interface resistance. THA-I exhibits the largest diameter and a higher R_{rec}, indicating that THA-I enhances charge carrier transport within the photoactive layer and reduces charge recombination between the photoactive layer and the Ag electrode. This observation is consistent with other results from charge recombination analyses.

The semicircular Nyquist plots for OSCs without an ETL, as well as those with a PDINN ETL and THA-I treatment are shown in Fig. S8c and S8d. The transport time (τ_{trans}) and recombination time (τ_{rec}) were directly derived from the frequency minimum point (f_{min}) of the semicircle at an angular frequency, using the relation τ_{trans} or $\tau_{rec} = 1/(2\pi f_{min})$.[18,19] The intensity-modulated photocurrent spectroscopy (IMPS) and intensity-modulated photovoltage

spectroscopy (IMVS) of the THA-I-treated device revealed a faster charge transfer lifetime and a longer charge recombination lifetime. The THA-I-treated device exhibited a faster τ_{trans} of 0.504 μs and a slower τ_{rec} of 6.34 μs compared to the device without an ETL (τ_{trans}=0.894 μs, τ_{rec}=3.99 μs) and the device with a PDINN ETL (τ_{trans}=0.564 μs, τ_{rec}=5.64 μs). These results are consistent with the TPC and TPV results (Fig. 3g and 3h), indicating that THA-I treatment promotes charge extraction and effectively inhibits charge recombination at the interface between the photoactive layer and the Ag electrode.

The charge collection efficiencies (η_{coll}), calculated using the relation η_{coll}=1-(τ_{trans}/τ_{rec}), were 77.6%, 90.0%, and 92.1% for the device without an ETL, the device with a PDINN ETL, and the THA-I-treated device, respectively. These results align with the η_{coll} values previously obtained from J_{ph}-V_{eff} analysis in Table S4 and demonstrate that THA-I treatment delays recombination at the interface between the photoactive layer and the Ag electrode, leading to more efficient charge extraction.

Adhesive interaction between the photoactive layer and electrode

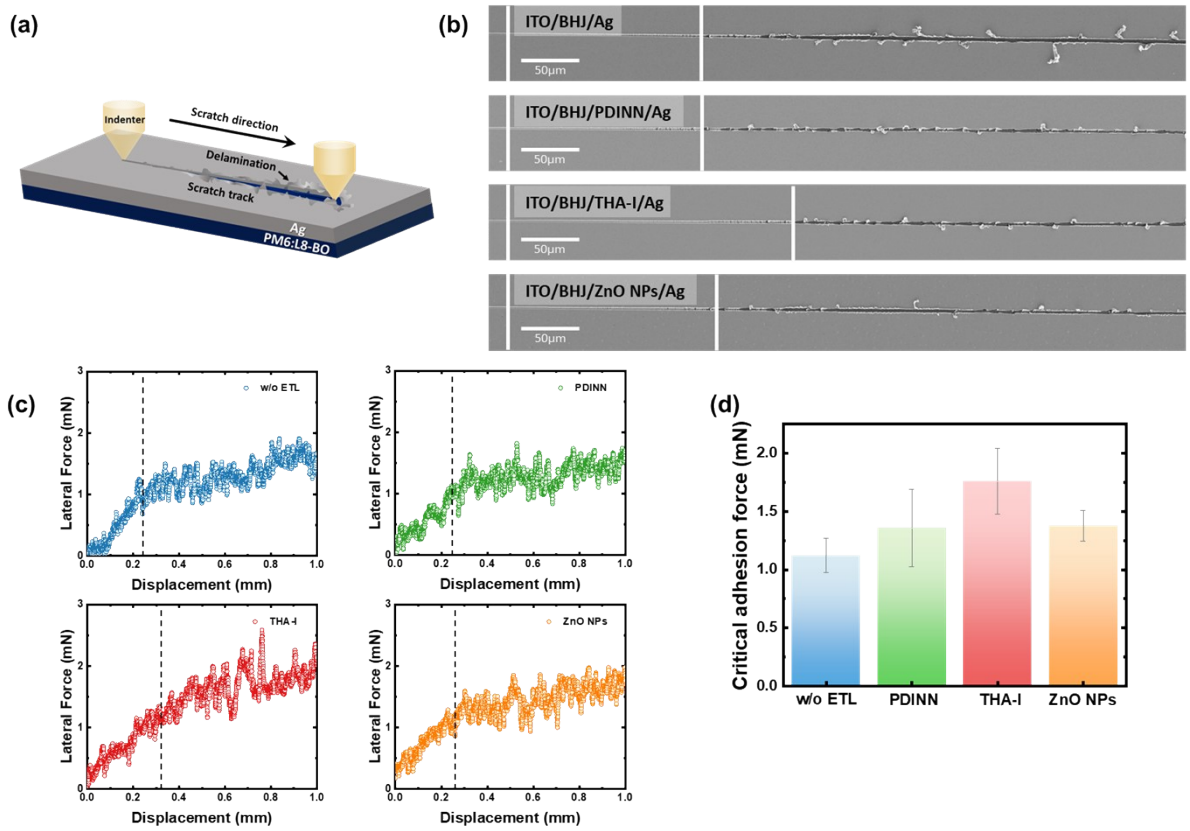

Figure S9. Nanoscratch test analysis of the adhesive interaction between PM6:L8-BO and Ag. (a) Schematic diagram of the nanoscratch test system used to evaluate critical adhesion, (b) SEM images of nanoscratch tracks on PM6:L8-BO/Ag films with or without an ETL, (c) variation in lateral force during the nanoscratch test on PM6:L8-BO/Ag films with or without an ETL, and (d) critical adhesion force between the PM6:L8-BO layer and the Ag electrode.

The adhesive interaction between the PM6:L8-BO photoactive layer and the Ag electrode was quantitatively measured using nanoscratch test analysis, depending on the type of ETL. As shown in the schematic diagram in Fig. S9a, the nanoscratch test involves applying vertical force to the indenter while gradually increasing the scratch depth until delamination occurs between the PM6:L8-BO layer and Ag. The lateral force measured at this point is defined as the critical adhesion force.[20]

The delamination point was determined by comparing changes in the lateral force with scanning electron microscope (SEM) images of the scratch track (Fig. S9b and S9c). The interaction between the PM6:L8-BO semiconductor material and the Ag metal primarily relies on weak physical interactions, such as van der Waals forces, resulting in low adhesion.[21, 22] As shown in Fig. S9d, PM6:L8-BO/Ag without an ETL exhibited the lowest critical adhesion force of 1.12 mN. Similarly, devices with PDINN and ZnO nanoparticle (ZnO NP) layers

inserted between PM6:L8-BO and Ag showed similarly low critical adhesion forces of 1.36 mN and 1.38 mN, respectively. The organic conductor PDINN may not sufficiently interact with the Ag electrode, while the metal oxide ZnO NPs may be limited in forming strong chemical bonds between PM6:L8-BO and Ag, resulting in low interfacial adhesion. In contrast, THA-I treatment between PM6:L8-BO and Ag improved the critical adhesion force to 1.76 mN, indicating that THA-I enhances interfacial adhesion. This improvement is attributed to the formation of AgI via chemical bonding between I^- ions from THA-I and the Ag surface, as confirmed by XPS results (Fig. 3).

Table S5. Average critical adhesion force values for the adhesive interaction between the PM6:L8-BO layer and the Ag electrode, depending on the type of ETL.

Sample	Average critical adhesion force (mN)
PM6:L8-BO/Ag	1.12±0.15
PM6:L8-BO/PDINN/Ag	1.36±0.33
PM6:L8-BO/THA-I/Ag	1.76±0.28
PM6:L8-BO/ZnO NPs/Ag	1.38±0.13

Organic thin film transistor (OTFT) measurements

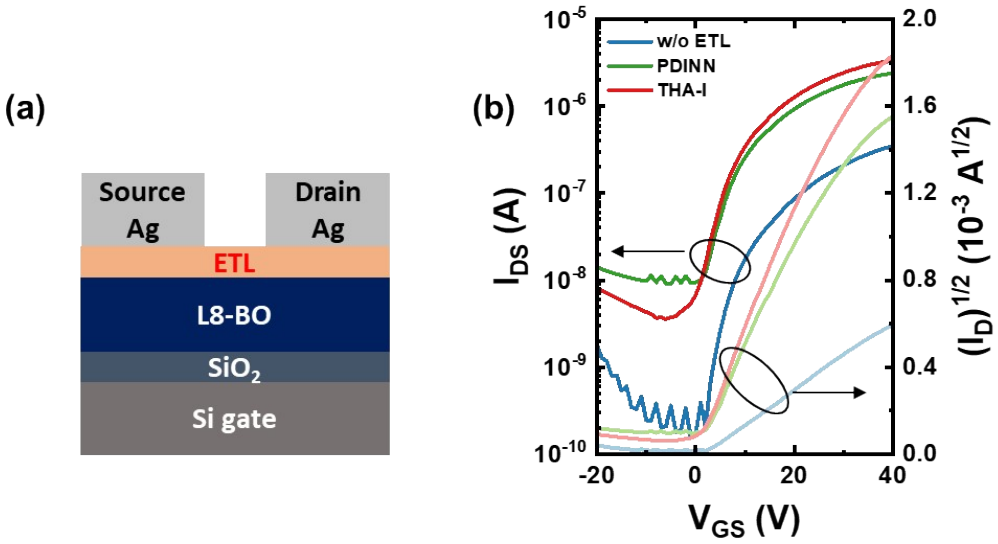

Figure S10. Organic thin-film transistor (OTFT) measurements for determining the electron mobility of L8-BO NFA. (a) Schematic device architecture of the OTFT and (b) OTFT transfer curves of L8-BO without an ETL, with PDINN, and with THA-I treatment.

To investigate charge transport properties, bottom-gate, top-contact OTFT devices were fabricated (Fig. S10a). As shown in Fig. S10b, a similar electron mobility trend was observed in OTFT measurements, consistent with the results of SCLC measurements. The L8-BO exhibited an electron mobility one order of magnitude higher compared to the device without an ETL. The device treated with THA-I showed consistent results across all mobility measurements, further supporting that THA-I facilitates electron transport. The charge mobility was calculated using the following equation:

$$\mu = \frac{2L}{WC_{ox}} \times \left(\frac{\partial\sqrt{I_{DS}}}{\partial V_{GS}}\right)^2,$$

where, I_{DS} is the drain current, μ is charge mobility, V_{GS} is the gate voltage, L is the channel length, W is the channel width and C_{ox} is the oxide capacitance.[23]

Table S6. Summary of transfer characteristics of L8-BO OTFTs.

L8-BO	μ_{OTFT} [cm²/V·s]	I_{on}/I_{off}	V_T [V]	I_{off} [A]	I_{on} [A]
w/o ETL	4.48×10^{-4}	1.49×10^{3}	1.83	3.01×10^{-12}	4.47×10^{-7}
PDINN	5.28×10^{-3}	2.61×10^{2}	-0.46	1.03×10^{-8}	2.68×10^{-6}
THA-I	6.94×10^{-3}	8.36×10^{2}	-1.28	4.43×10^{-9}	3.71×10^{-6}

MSM type-I device stability test

▪ Photo-stability without encapsulation

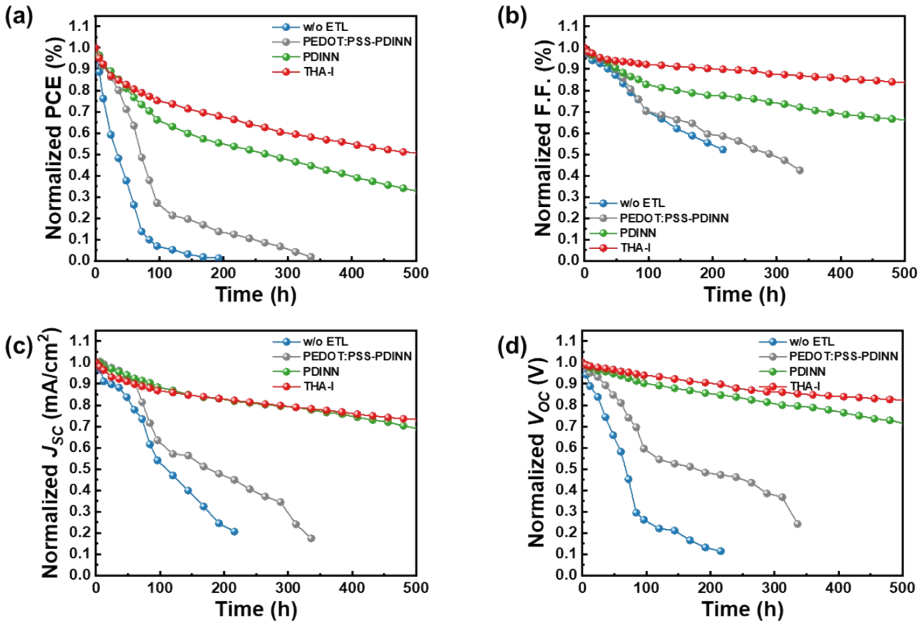

Figure S11. Normalized photovoltaic parameters of the quasi-MSM type-I device under continuous illumination with MPP tracking at 25 °C and 20% RH, without encapsulation: (a) PCE, (b) FF, (c) J_{SC} and (d) V_{OC}.

▪ Photo-stability with encapsulation

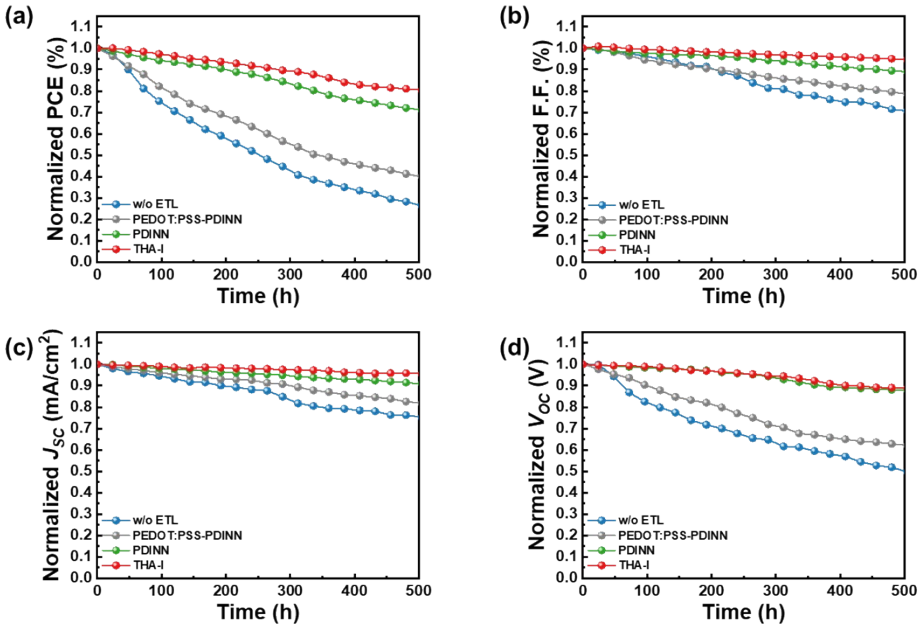

Figure S12. Normalized photovoltaic parameters of the encapsulated quasi-MSM type-I device under continuous illumination with MPP tracking at 25 °C and 20% RH: (a) PCE, (b) FF, (c) J_{SC} and (d) V_{OC}.

▪ **Thermal stability without encapsulation**

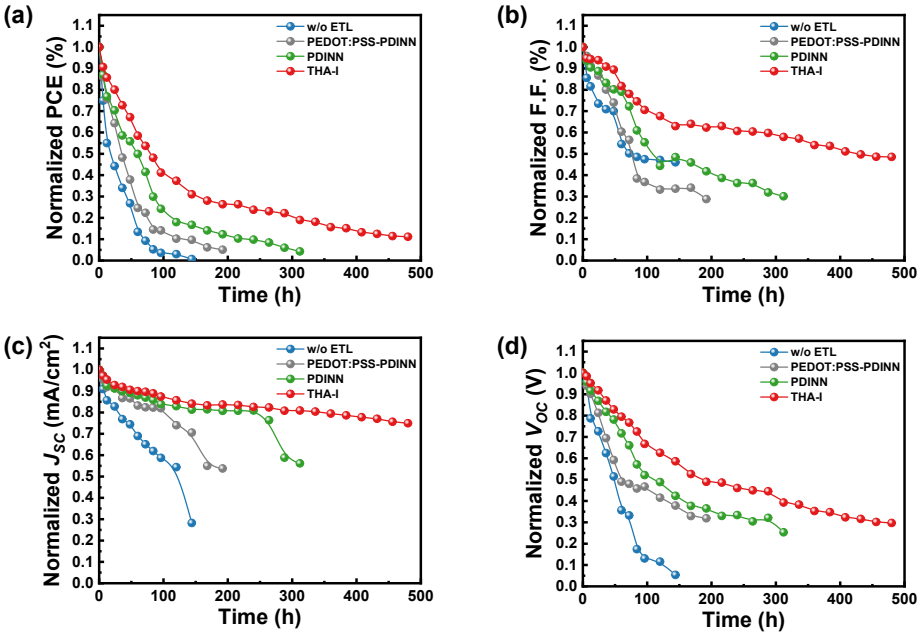

Figure S13. Normalized photovoltaic parameters of the quasi-MSM Type-I device at 65 ℃ and 65% RH: (a) PCE, (b) FF, (c) J_{SC} and (d) V_{OC}.

▪ **Thermal stability with encapsulation**

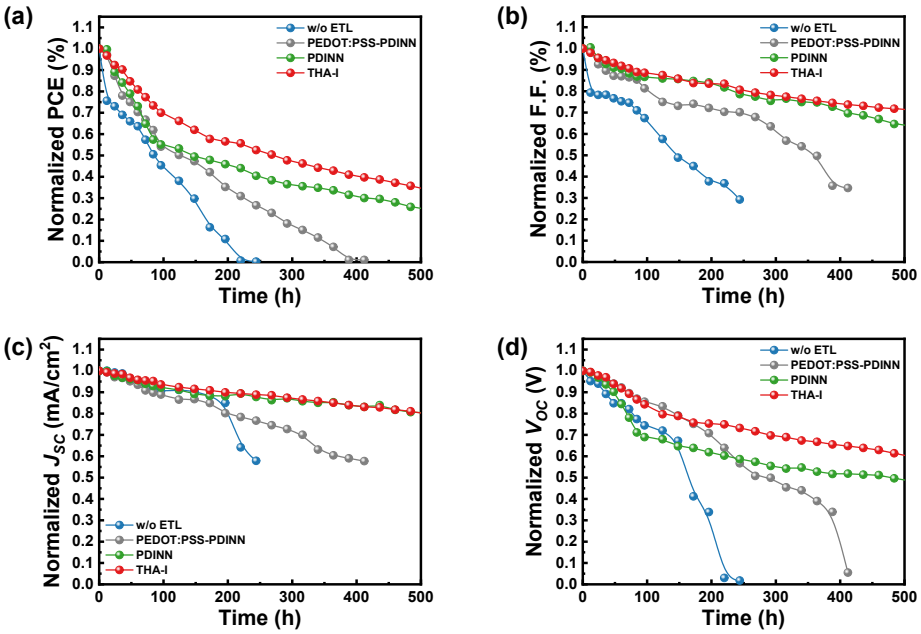

Figure S14. Normalized photovoltaic parameters of the encapsulated quasi-MSM Type-I device at 65 ℃ and 65% RH: (a) PCE, (b) FF, (c) J_{SC} and (d) V_{OC}.

To evaluate the long-term photo- and thermal stability of the type-I device, maximum power point (MPP) tracking was conducted under controlled temperature and humidity conditions. Non-encapsulated and encapsulated devices were tested at 25 °C/20% RH using a solar cell reliability test system (K3600, McScience Inc.) and at 65 °C/65% RH using a temperature–humidity chamber (TH-ME, JEIO TECH).

As shown in Fig. S11 to S14, conventional OSCs employing PEDOT:PSS as the HTL and PDINN as the ETL (PEDOT:PSS-PDINN) exhibited the second fastest degradation in performance under all tested conditions, following the device without an ETL. This degradation is primarily attributed to PEDOT:PSS, which, due to its acidity, can corrode the ITO anode in the presence of moisture and oxygen.[24,25] Its hygroscopic nature also promotes water uptake, accelerating reactions with the metal electrode and photoactive layer and thus hastening device failure. PDINN similarly suffers from sensitivity to moisture and oxygen; its structural and electrochemical properties deteriorate upon prolonged exposure. Furthermore, light or thermal stress above 65 °C can alter the conductivity and energy level alignment of PDINN, reducing electron extraction efficiency and increasing interfacial resistance.[26] Consequently, devices using PDINN ETLs exhibit poor stability, particularly under non-encapsulated conditions (Fig. S11 and S13), underscoring the instability of the PDINN interface.

In contrast, devices treated with THA-I demonstrated improved stability under all conditions, despite requiring only simple interfacial treatment. Specifically, MPP tracking of the encapsulated device under simulated 1 sun at 25 °C/20% RH showed that the THA-I-treated device retained 67.3% of its initial PCE after 500 hours, outperforming both the ETL-free device (16.9%) and the PDINN-based device (51.6%) (Fig. S12). Similarly, under thermal aging at 65 °C/65% RH without encapsulation, the THA-I-treated device maintained superior performance over 500 hours (Fig. S13). This enhanced stability is attributed to the formation of a chemically bonded AgI interfacial layer, induced by THA-I, which strengthens electrode adhesion and suppresses interfacial degradation.

Time-dependent morphological evolution of PM6:L8-BO

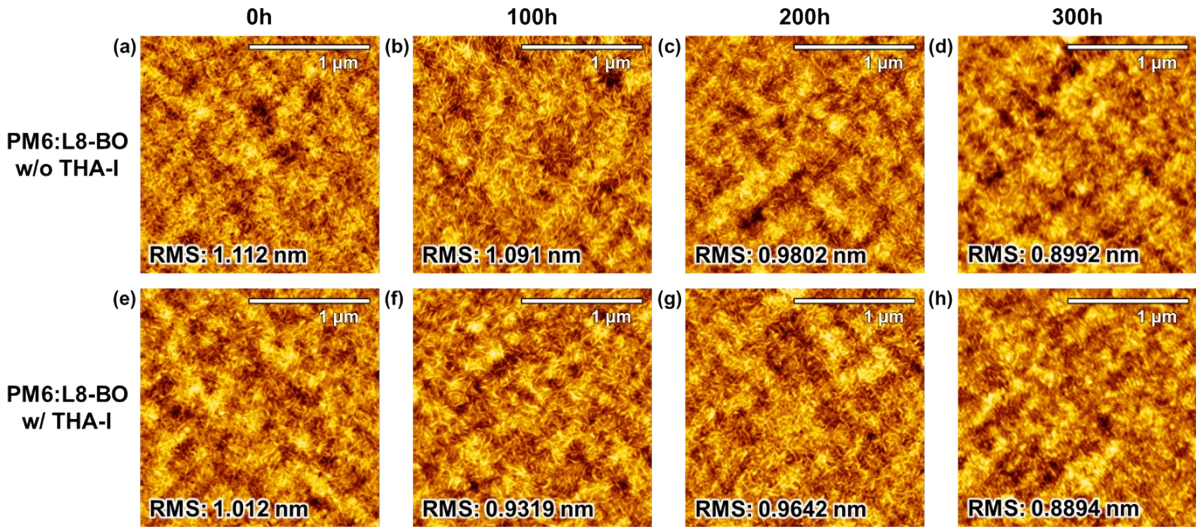

Figure S15. AFM surface images (2 μm x 2 μm) of PM6:L8-BO films (a-d) without THA-I and (e-h) with THA-I after various storage durations inside a glove box.

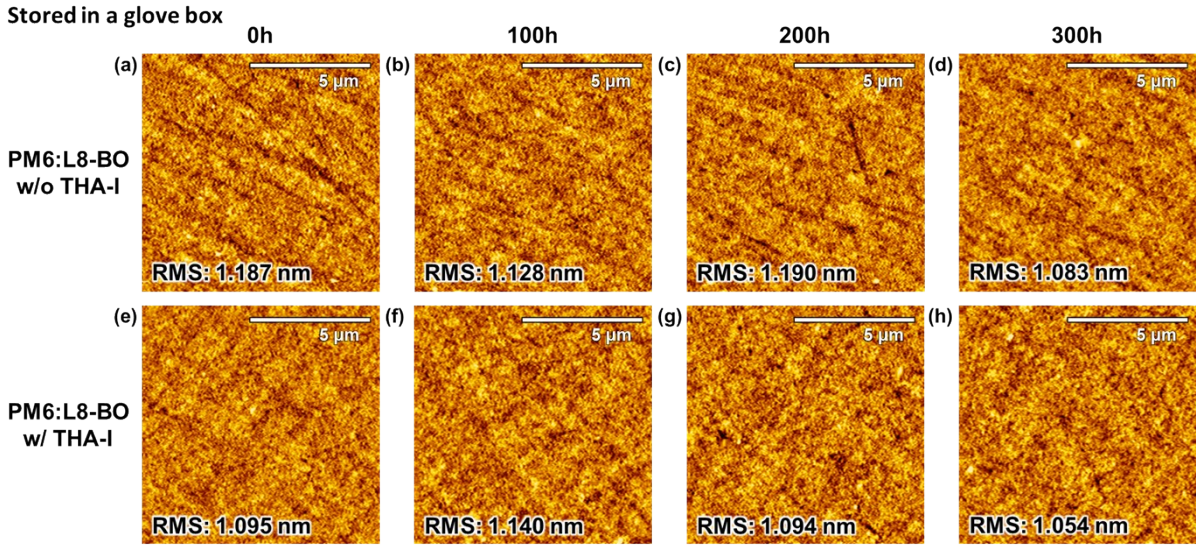

Figure S16. AFM surface images (10 μm x 10 μm) of PM6:L8-BO films (a-d) without THA-I and (e-h) with THA-I after various storage durations inside a glove box.

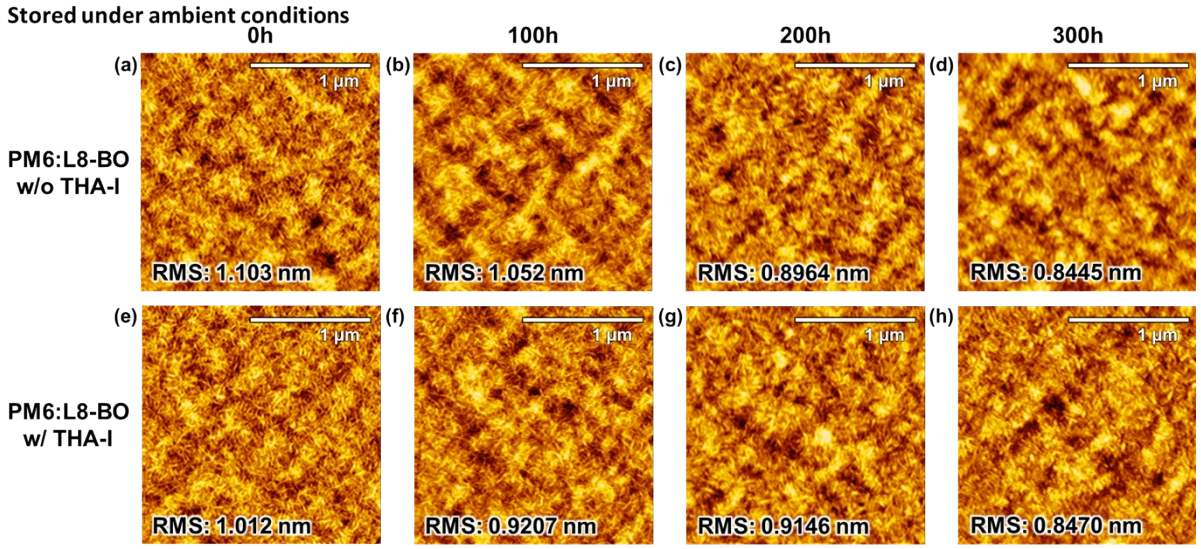

Figure S17. AFM surface images (2 μm x 2 μm) of PM6:L8-BO films (a-d) without THA-I and (e-h) with THA-I after various storage durations under ambient conditions.

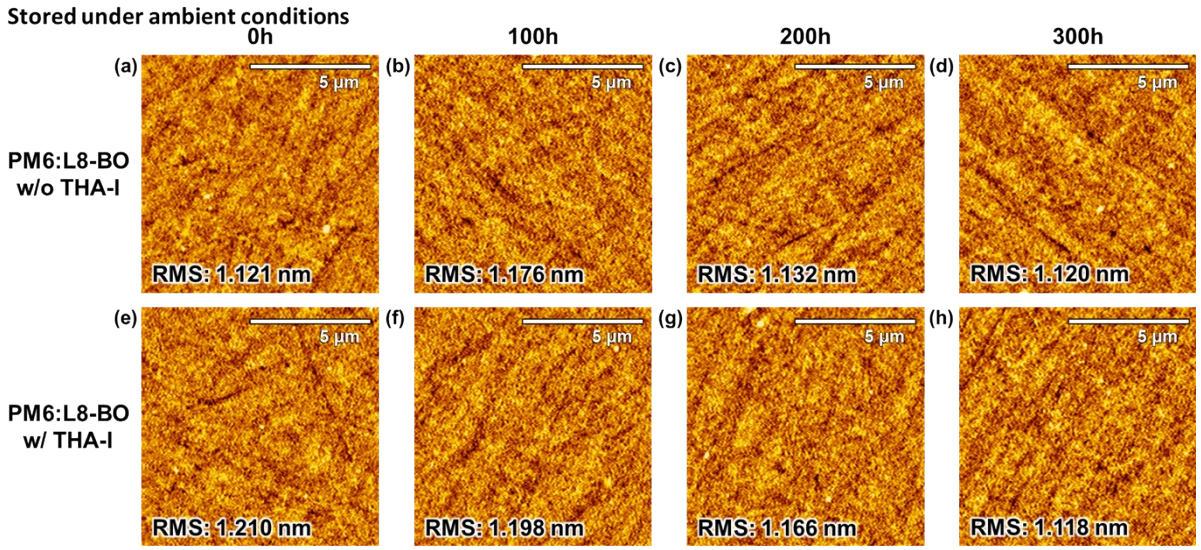

Figure S18. AFM surface images (10 μm x 10 μm) of PM6:L8-BO films (a-d) without THA-I and (e-h) with THA-I after various storage durations under ambient conditions.

To investigate the time-dependent morphological evolution of PM6:L8-BO with and without THA-I treatment, AFM measurements were performed under different storage conditions. Both treated and untreated samples exhibited a gradual decrease in RMS roughness from ~1.1 nm to below 0.9 nm over time. This steady trend suggests slow fibril relaxation, with no abrupt changes indicative of phase separation or degradation (Fig. S15 and S17). Similarly, large-area AFM scans (Fig. S16 and S18) revealed no significant morphological differences associated with THA-I treatment, indicating that it does not adversely affect the photoactive layer morphology during storage.

MSM type-II devices based on PTB7-Th:IEICO-4F

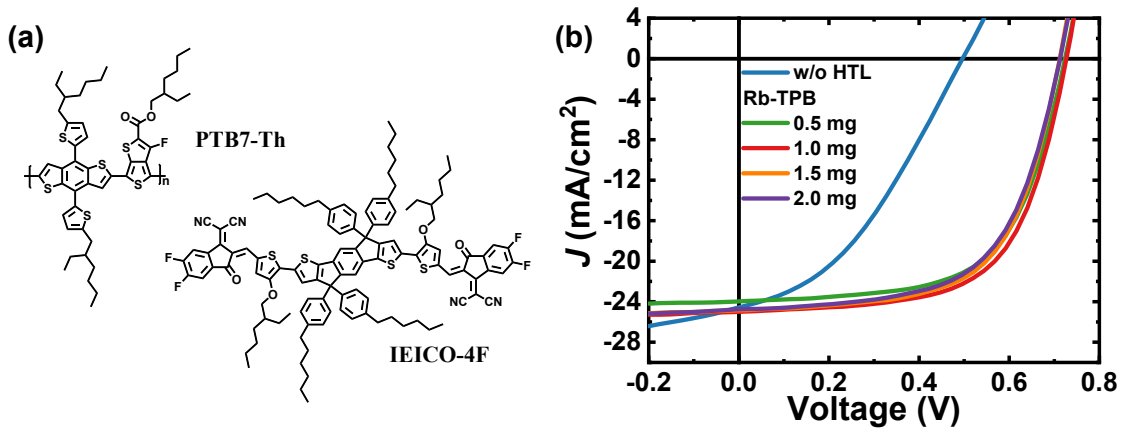

Figure S19. (a) Chemical structures of the p-type polymer PTB7-Th and the non-fullerene acceptor IEICO-4F, (b) *J-V* characteristics of MSM type-II devices based on PTB7-Th:IEICO-4F with different concentrations of Rb-TPB.

Table S7. Photovoltaic performance parameters of MSM type-II devices based on PTB7-Th:IEICO-4F with varying concentrations of Rb-TPB dissolved in chlorobenzene (CB).

Concentration in CB	V_{OC} [V]	J_{SC} [mA/cm²]	F.F. [%]	PCE [%]
w/o HTL	0.496	24.56	38.25	4.66
Rb-TPB 0.5 mg/ml	0.724	23.97	62.10	10.77
Rb-TPB 1.0 mg/ml	0.727	25.00	62.71	11.40
Rb-TPB 1.5 mg/ml	0.712	24.85	62.11	11.00
Rb-TPB 2.0 mg/ml	0.713	24.74	60.75	10.72

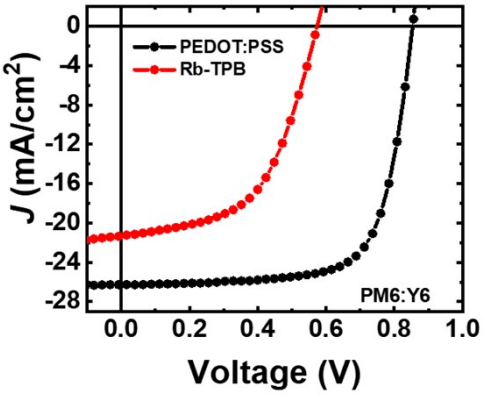

Figure S20. *J-V* characteristics of MSM type-II devices based on PM6:Y6 incorporating Rb-TPB

Table S8. Photovoltaic performance parameters of MSM type-II devices based on PM6:Y6 incorporating Rb-TPB

	V_{OC} [V]	J_{SC} [mA/cm^2]	F.F. [%]	Best PCE [%]
PEDOT:PSS	0.853	26.27	71.75	16.09
Rb-TPB	0.574	21.32	54.23	6.64

Non-modulated impedance spectroscopy for MSM type-II devices

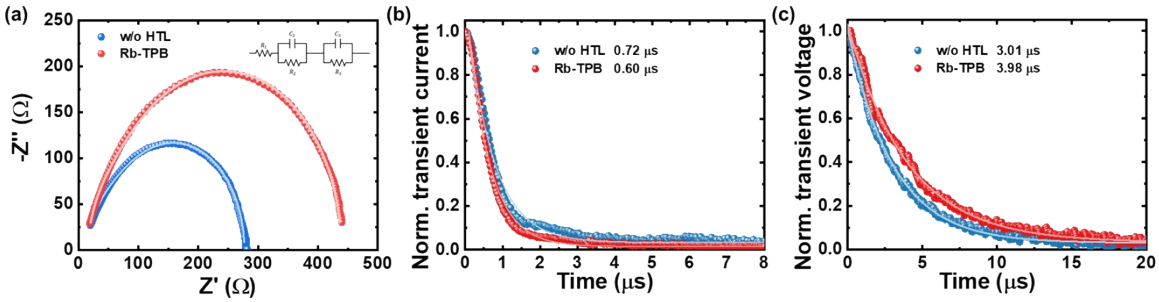

Figure S21. (a) Non-modulated impedance spectroscopy (IS), (b) TPC, and (c) TPV measurements conducted on MSM type-II devices based on PTB7-Th:IEICO-4F with Rb-TPB.

Non-modulated IS for the MSM type-II device was measured in the dark under open-circuit conditions. The spectra were fitted according to the equivalent electric circuit shown in the inset.[27] The series resistance (R_S) was considered the contact resistance. A constant phase element (CPE) was used to model the capacitance in non-ideal systems, and the recombination time (τ_{rec}) was defined as $\tau_{rec}=R_{rec}C_{\mu}$.[28,29]

From the extracted parameters shown in Table S9, the device using Rb-TPB exhibited better charge transport and recombination properties compared to the ITO-only device. The fitted recombination resistance (R_{rec}) for the ITO-only device was 277.2 Ω, which is lower than the 446.4 Ω observed in the Rb-TPB device. The higher R_{rec} values in the Rb-TPB device indicate a lower rate of charge recombination, suggesting that recombination was more pronounced in the ITO-only device.

This improvement trend was also observed in TPV and TPC measurements. From the TPC analysis, the device using Rb-TPB exhibited a lower transport time of 0.61 μs compared to 0.77 μs for the ITO-only device, indicating better charge extraction in the Rb-TPB device. Additionally, the Rb-TPB device showed an increased charge recombination time of 3.98 μs, confirming a lower charge recombination rate compared to the ITO-only device (3.01 μs). Overall, both measurement techniques confirm the superior electrical properties of the device using Rb-TPB.

Table S9. Parameters extracted by fitting the impedance spectra of the MSM type-II device to the equivalent circuit.

Device	R_s [Ω]	R_t [Ω]	C_t [nF]	R_{rec} [Ω]	C_{μ} [nF]
w/o HTL	16.45	213.1	11.29	47.53	10.68
Rb-TPB	16.03	371.5	9.173	51.16	11.84

MSM type-II device stability test

▪ Photo-stability without encapsulation

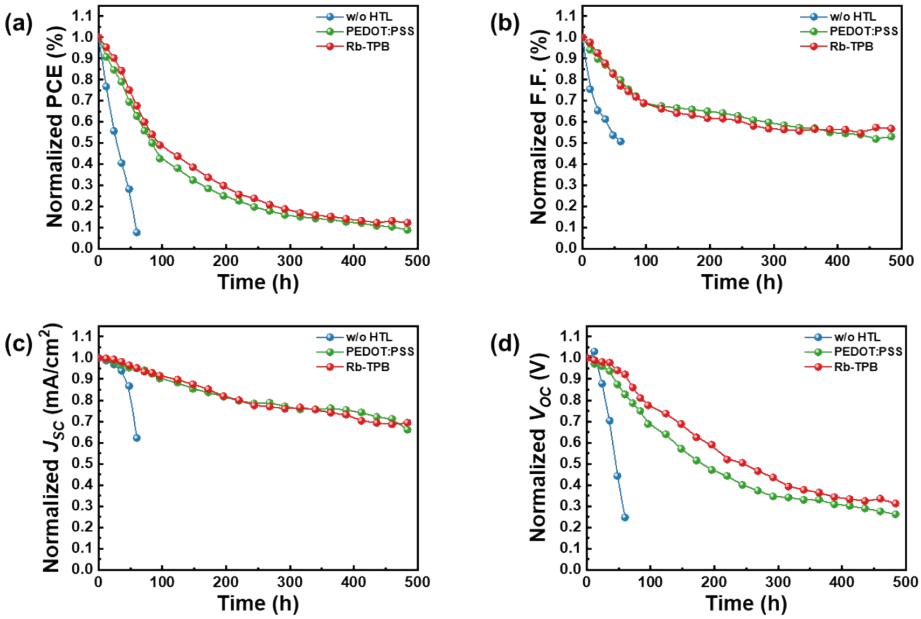

Figure S22. Normalized photovoltaic parameters of the MSM Type-II device under continuous illumination with MPP tracking at 25 ℃ and 20% RH: (a) PCE, (b) FF, (c) J_{SC} and (d) V_{OC}.

▪ Photo-stability with encapsulation

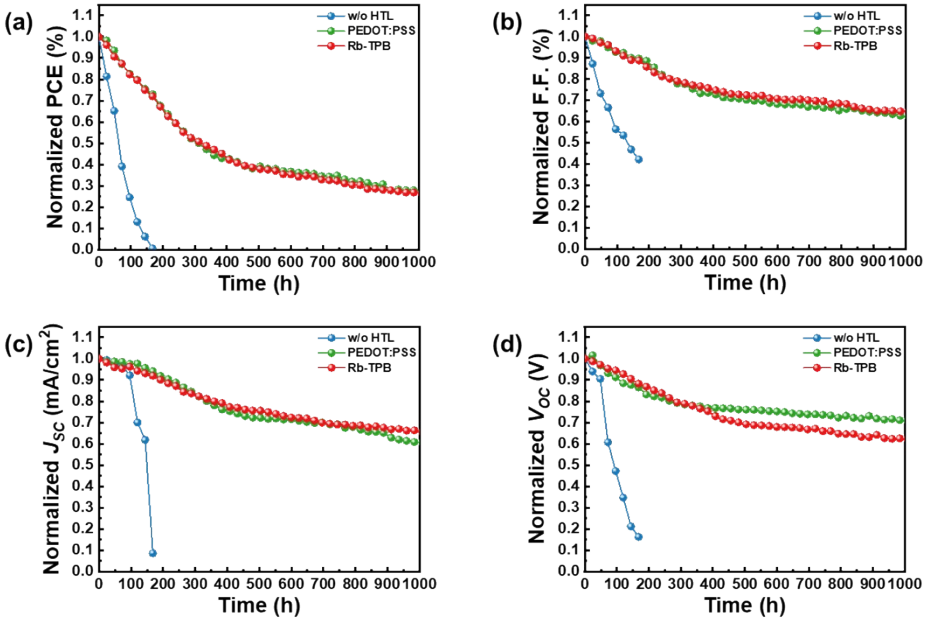

Figure S23. Normalized photovoltaic parameters of the encapsulated MSM Type-II device under continuous illumination with MPP tracking at 25 ℃ and 20% RH: (a) PCE, (b) FF, (c) J_{SC} and (d) V_{OC}.

▪ Thermal stability without encapsulation

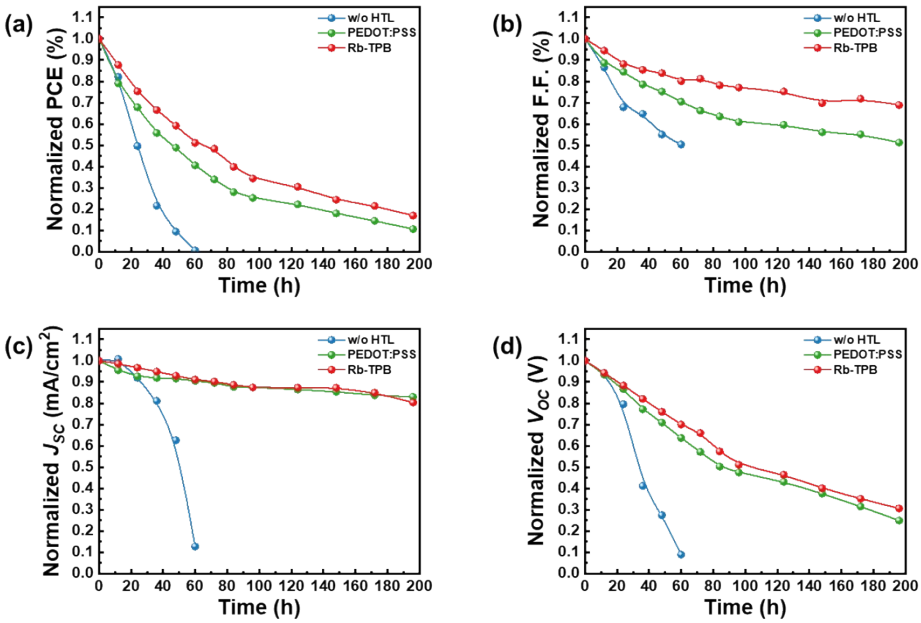

Figure S24. Normalized photovoltaic parameters of the MSM Type-II device at 65 ℃ and 65% RH: (a) PCE, (b) FF, (c) J_{SC} and (d) V_{OC}.

▪ **Thermal stability with encapsulation**

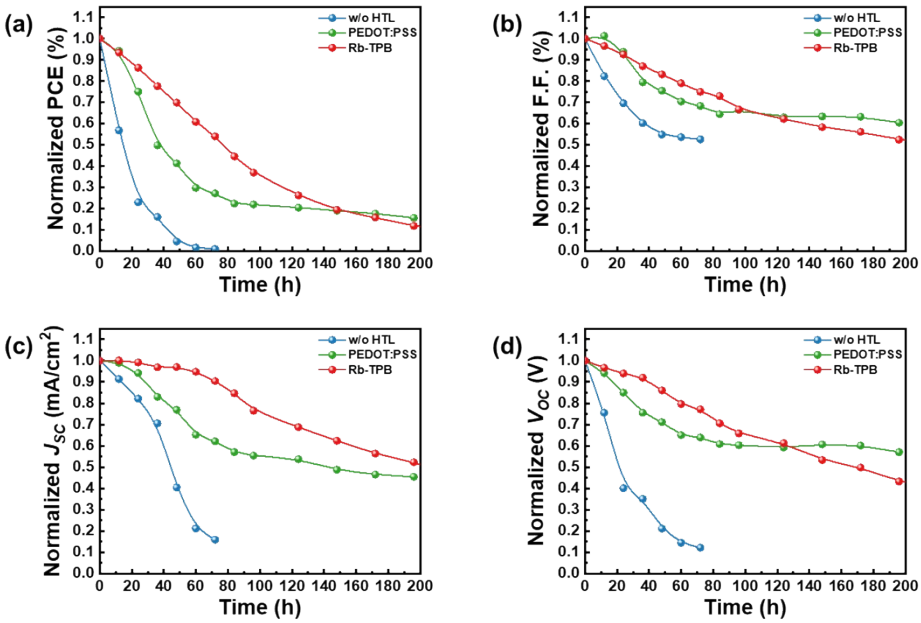

Figure S25. Normalized photovoltaic parameters of the encapsulated MSM Type-II device at 65 ℃ and 65% RH: (a) PCE, (b) FF, (c) J_{SC} and (d) V_{OC}.

To evaluate the long-term photo- and thermal stability of the type-II device, maximum power point (MPP) tracking was conducted under controlled temperature and humidity conditions. As shown in Fig. S22 to S25, the device without an HTL exhibited rapid performance degradation under all tested conditions. PEDOT:PSS-based devices also showed poor stability, primarily due to the acidic nature of PEDOT:PSS, which can corrode the ITO anode, and its strong hygroscopicity, which promotes moisture uptake and subsequent degradation of both the metal electrode and the photoactive layer. As a result, device degradation was significantly accelerated. Although devices incorporating Rb-TPB showed improved thermal stability at 65 °C/65% RH, their overall stability remained poor and comparable to that of PEDOT:PSS-based devices. These results highlight the need for developing p-type interfacial materials that offer both favorable energy level alignment and resistance to moisture and thermal stress for achieving stable, high-performance MSM OSCs.

The MSM type-III device

Table 10. Photovoltaic parameters of the MSM type-III device.

HTL	Photoactive layer	V_{OC} [V]	J_{SC} [mA/cm^2]	F.F. [%]	PCE [%]	PCE_{Avg} [%]
-	PM6:Y6	0.553	23.09	64.96	8.293	7.60±0.50
PEDOT:PSS	PM6:Y6	0.851	25.70	73.07	15.98	15.73±0.22
-	PM6:Y6+PTA 5%	0.835	25.64	75.72	16.20	16.06±0.17

Interfacial morphology of MSM type-III photoactive layers with and without PTA.

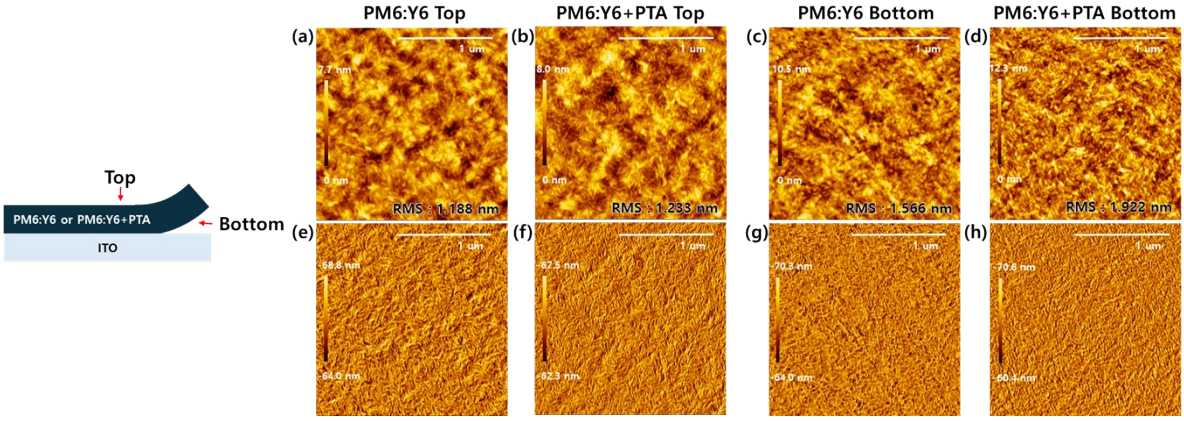

Figure S26. (a–d) AFM surface topography images (2 μm x 2 μm) showing the top and bottom interfaces of PM6:Y6 films without and with PTA. (e–h) Corresponding AFM phase images.

Device characterization of the MSM type-III device

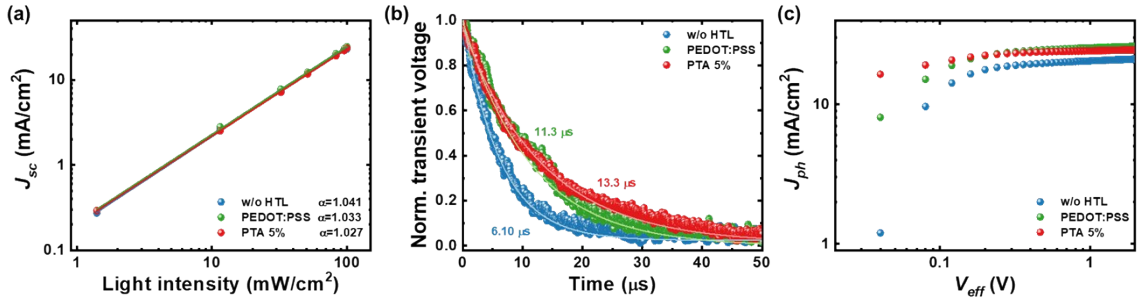

Figure S27. (a) Light intensity dependence of J_{SC}, (b) TPV, and (c) J_{ph} -V_{eff} measurements for the MSM type-III device.

The α value in Fig. S27a represents how J_{SC} responds to changes in light intensity, with values close to 1 indicating minimal bimolecular recombination. The device without an HTL exhibited the highest α value of 1.041, suggesting increased bimolecular recombination.[7] This is further confirmed by the shortest recombination time of 6.098 μs in the TPV analysis (Fig. S27b), indicating faster charge recombination at the interface and reduced charge extraction efficiency. In contrast, the device with a PEDOT:PSS HTL exhibited a more favorable α value of 1.033 and a longer recombination time of 11.3 μs, indicating improved charge transport and reduced recombination losses. Similarly, the device using PTA showed the lowest α value of 1.027 and the longest recombination time of 13.3 μs, demonstrating the most effective suppression of recombination losses among the three devices.

Further insights into the exciton generation rate (G_{max}) and exciton dissociation efficiency (η_{diss}) are provided in Fig. S27c. Detailed G_{max} and η_{diss} values for these devices are summarized in Table S10. The device without an HTL showed the lowest G_{max} of 1.58×10^{26} m^{-3} s^{-1} and η_{diss} of 93.4%, leading to inefficient charge separation and poor device performance (Table S10).[30] In contrast, the device with a PEDOT:PSS HTL exhibited a significantly higher G_{max} of 1.63×10^{27}m^{-3}s^{-1} and η_{diss} of 96.9%, reflecting improved charge transport and exciton dissociation. Although the device using PTA showed a slight reduction in G_{max} of 1.55×10^{27}m^{-3}s^{-1}, it maintained a high η_{diss} of 96.7%, resulting in overall performance comparable to the device using PEDOT:PSS HTL. These results align with the observations from IS, IMPS, and IMVS measurements, as shown in Fig. S28.

Table S11. Exciton generation rate (G_{max}) and exciton dissociation efficiency (η_{diss}) of the MSM type-III device calculated from J_{ph}-V_{eff} measurements.

HTL	Photoactive layer	G_{max} [m^{-3} s^{-1}]	η_{diss} [%]
-	PM6:Y6	1.58×10^{26}	93.4
PEDOT:PSS	PM6:Y6	1.63×10^{27}	96.9
-	PM6:Y6+PTA 5%	1.55×10^{27}	96.7

Non-modulated impedance spectroscopy for MSM type-III devices

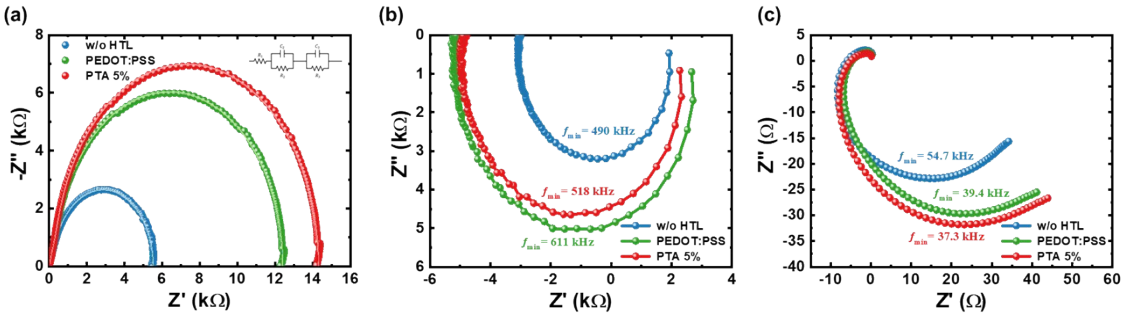

Fig. S28. (a) Non-modulated impedance spectroscopy under dark conditions, (b) IMPS, and (c) IMVS of the MSM type-III.

The Nyquist plot shown in Fig. S28a was fitted to the equivalent electric circuit depicted in the inset. The diameter of the semicircle represents the charge recombination resistance (R_{rec}), with a larger R_{rec} typically indicating a lower charge recombination rate. The device using PTA demonstrated a larger semicircle (higher R_{rec}) compared to the device using PEDOT:PSS, suggesting effective suppression of charge recombination at the interface.

The charge transport lifetime (τ_{trans}) and recombination lifetime (τ_{rec}) of the MSM type-III device were determined through IMPS and IMVS measurements. These lifetimes were calculated using the equation $\tau = 1/(2\pi f_{min})$, where f_{min} refers to the frequency at the minimum of the semicircle, as summarized in Table S13.[18,19] The device with PTA exhibited a longer τ_{trans} of 0.307 μs compared to 0.261 μs for the device with PEDOT:PSS, implying that PTA impedes charge separation and transport. Additionally, the increase in τ_{rec} for the device using PTA (4.269 μs) compared to that of the PEDOT:PSS HTL device (4.042 μs) further confirms a reduction in charge recombination.

The results from IS, IMPS, and IMVS indicate that incorporating PTA effectively suppresses charge recombination at the interface between the photoactive layer and the ITO electrode. The calculated charge collection efficiencies were 86.1% for devices without an HTL, 91.9% for

devices using PEDOT:PSS HTL, and 91.5% for devices using PTA. Notably, devices with PTA and PEDOT:PSS HTL exhibited comparable charge collection efficiencies.

Table S12. The parameters extracted by fitting the impedance spectra of the MSM type-III device with the equivalent circuit.

HTL	Photoactive layer	R_s [Ω]	R_t [Ω]	C_t [nF]	R_{rec} [kΩ]	C_μ [nF]
-	PM6:Y6	66.44	189.8	6.386	5.260	2.565
PEDOT:PSS	PM6:Y6	59.14	302.0	5.723	12.04	2.533
-	PM6:Y6+PTA 5%	41.68	292.5	5.008	13.96	2.588

Table S13. Charge transport time (τ_{trans}), recombination time (τ_{rec}) and charge collection efficiency (η_{coll}) of the MSM type-III device calculated from IMPS and IMVS.

HTL	Photoactive layer	τ_{trans} [μs]	τ_{rec} [μs]	η_{coll} [%]
-	PM6:Y6	0.325	2.909	86.1
PEDOT:PSS	PM6:Y6	0.261	4.042	91.9
-	PM6:Y6+PTA 5%	0.307	4.269	91.5

MSM type-III device stability test

▪ Photo-stability without encapsulation

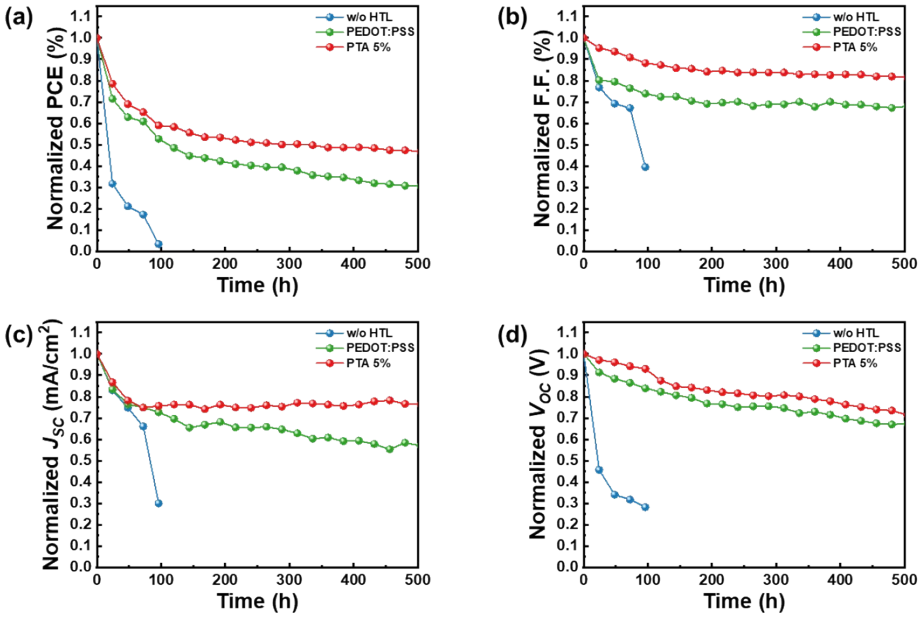

Figure S29. Normalized photovoltaic parameters of the MSM Type-III device under continuous illumination with MPP tracking at 25 ℃ and 20% RH: (a) PCE, (b) FF, (c) J_{SC} and (d) V_{OC}.

▪ Photo-stability with encapsulation

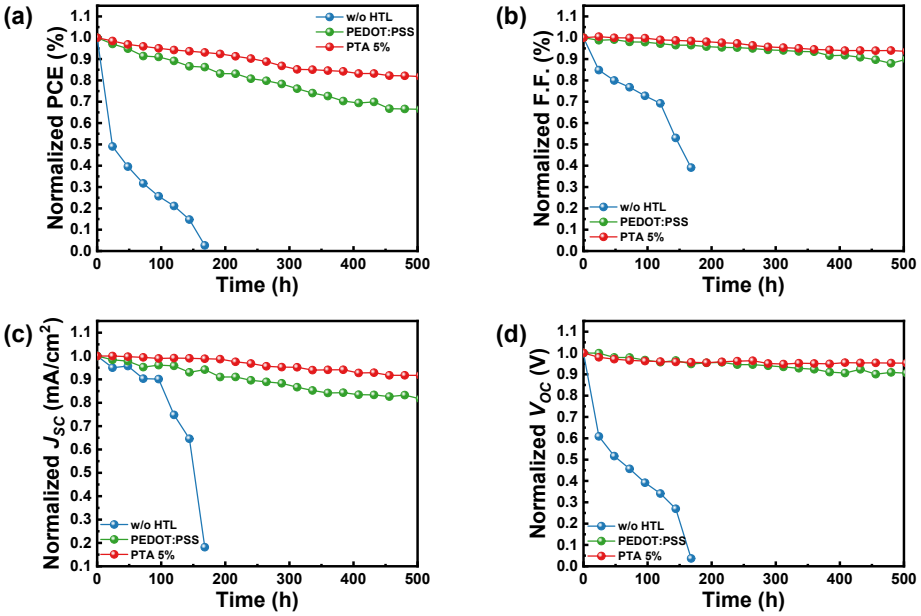

Figure. S30. Normalized photovoltaic parameters of the encapsulated MSM Type-III device under continuous illumination with MPP tracking at 25 ℃ and 20% RH: (a) PCE, (b) FF, (c) J_{SC} and (d) V_{OC}.

▪ Thermal stability without encapsulation

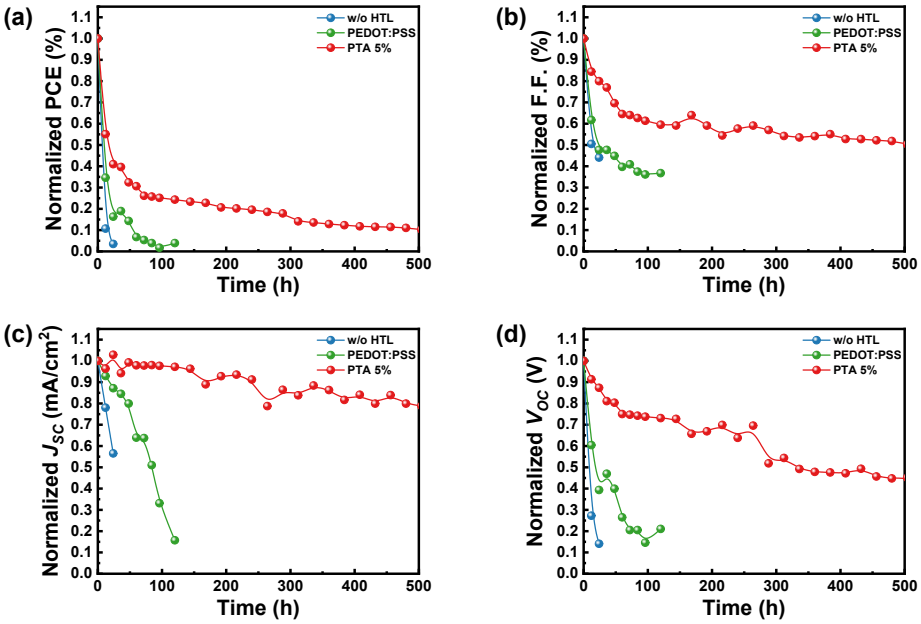

Figure S31. Normalized photovoltaic parameters of the MSM Type-III device at 65 °C and 65% RH: (a) PCE, (b) FF, (c) J_{SC} and (d) V_{OC}.

▪ **Thermal stability with encapsulation**

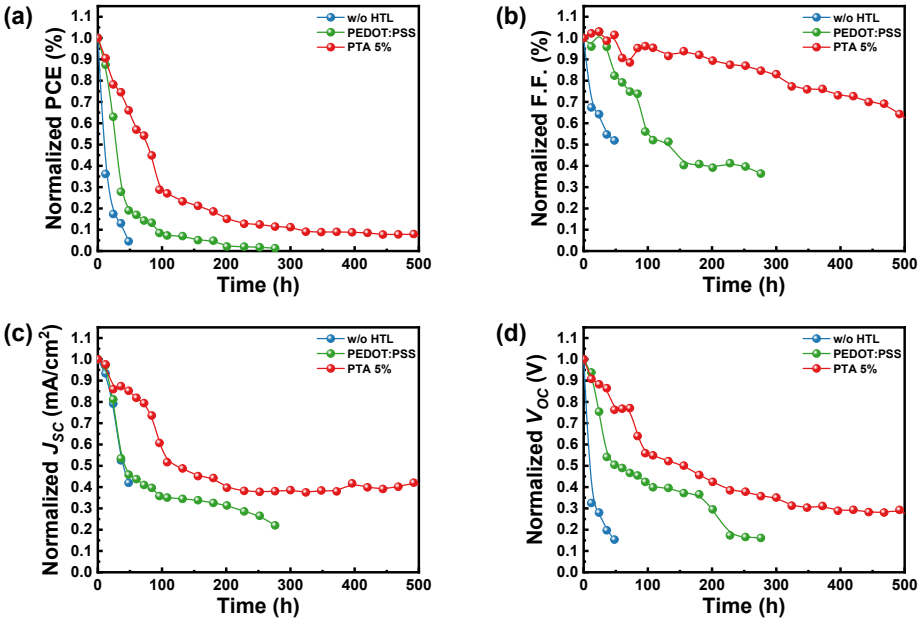

Figure S32. Normalized photovoltaic parameters of the encapsulated MSM Type-III device at 65 °C and 65% RH: (a) PCE, (b) FF, (c) J_{SC} and (d) V_{OC}.

To evaluate the long-term photo- and thermal stability of the type-III device, maximum power point (MPP) tracking was conducted under controlled temperature and relative humidity (RH)

conditions. As shown in Fig. S29 to S32, the device without an HTL exhibited rapid degradation under all conditions, particularly at 65 °C/65% RH. The PEDOT:PSS-based device showed relatively stable performance at 25 °C/25% RH (Fig. S29 and S30), but degraded rapidly at 65 °C/65% RH (Fig. S31 and S32). In contrast, the device incorporating PTA exhibited the highest stability across all tested conditions. Under encapsulated conditions at 25 °C/25% RH, the PTA-based device retained over 80% of its initial FF, J_{SC}, and V_{OC} after 1000 hours. Notably, even under the harsh, non-encapsulated 65 °C/65% RH condition, the device maintained more than 50% of its initial FF, J_{SC}, and V_{OC} after 500 hours, while the devices without an HTL and with PEDOT:PSS degraded completely. These results clearly demonstrate that PTA incorporation significantly enhances the environmental and thermal robustness of OSCs, even in the absence of encapsulation.

Data for Module device

Table S14. Photovoltaic performance parameters of MSM type-I module devices.

HTL	V_{OC} [V]	J_{SC} [mA/cm^2]	F.F.	PCE [%]
PEDOT:PSS	9.31	2.30	64.96	13.94
SAM	8.36	2.29	44.10	8.48

Table S15. Photovoltaic performance parameters of MSM type-III module devices.

HTL	Photoactive layer	V_{OC} [V]	J_{SC} [mA/cm^2]	F.F.	PCE [%]
PEDOT:PSS	PM6:Y6	9.22	2.28	65.06	13.69
PTA	PM6:Y6	9.31	2.32	68.70	14.89
-	PM6:Y6	7.51	2.37	43.04	7.69
-	PM6:Y6+PTA	9.28	2.33	67.22	14.54

ETL: THA-I, Active area: 54 cm^2

Table S16. Comparison of representative HTL- and/or ETL-free organic solar cells reported in recent literature, highlighting device architecture, power conversion efficiency, stability metrics, and fabrication complexity, together with the Type-III MSM devices demonstrated in this work.

	Device structure	BHJ	PCE (%)	Device stability
Ref.	**ETL-Free**			
31	Glass/A-IAI/BHJ/PEDOT:PSS/Ag	P3HT:$PC_{61}BM$	2.66	-
32	ITO-serine/BHJ/MoO_3/Al	P3HT:$PC_{61}BM$	4.17	-
33	Glass/ITO/BHJ/MoO_3/Ag	P3HT:$PC_{71}BM$:PDTFN	3.58	-
34	Glass/ITO/PEDOT:PSS/BHJ/eutectic gallium-indium	PM6:Y6	14.1	-
	HTL-free			
35	ITO-CF_3-SAM/BHJ/LiF/Ag	P3HT:$PC_{61}BM$	3.15	-
36	ITO-Cl/BHJ/F3N-Br/Ag	PM6:L8-BO:BTP-eC9	19.48	Storing in N_2 filled GB, after 200 h, Storage: 88% of initial PCE 1 Sun illum.: 62.1%of initial PCE Thermal(T85): 35.4% of initial PCE

References

1. T. Hahn, S. Tscheuschner, F.-J. Kahle, M. Reichenberger, S. Athanasopoulos, C. Saller, G. C. Bazan, T.-Q. Nguyen, P. Strohriegl, H. Bässler and A. Köhler, *Adv. Funct. Mater.*, 2017, **27**, 1604906.
2. G.-J. A. H. Wetzelaer, M. Scheepers, A. M. Sempere, C. Momblona, J. Ávila and H. J. Bolink, *Adv. Mater.*, 2015, **27**, 1837.
3. P. W. M. Blom, M. J. M. De Jong and J. J. M. Vleggaar, Appl. Phys. Lett., 1996, 68, 3308.
4. G. Zhang, X.-K. Chen, J. Xiao, P. C. Y. Chow, M. Ren, G. Kupgan, X. Jiao, C. C. S. Chan, X. Du, R. Xia, Z. Chen, J. Yuan, Y. Zhang, S. Zhang, Y. Liu, Y. Zou, H. Yan, K. S. Wong, V. Coropceanu, N. Li, C. J. Brabec, J.-L. Brédas, H.-L. Yip and Y. Cao, *Nat. Commun.*, 2020, **11**, 3943.
5. C. Zhan, X. Zhang and J. Yao, *RSC Adv.*, 2015, **5**, 93002.
6. V. D. Mihailetchi, J. Wildeman and P. W. M. Blom, *Phys. Rev. Lett.*, 2005, **94**, 126602.
7. J.-L. Wu, F.-C. Chen, Y.-S. Hsiao, F.-C. Chien, P. Chen, C.-H. Kuo, M. H. Huang and C.-S. Hsu, *ACS Nano*, 2011, **5**, 959.
8. Y. Wang, F. Wang, J. Gao, Y. Yan, X. Wang, X. Wang, C. Xu, X. Ma, J. Zhang and F. Zhang, *J. Mater. Chem. C*, 2021, **9**, 9892.
9. M. Jiang, H. Bai, H. Zhi, L. Yan, H. Y. Woo, L. Tong, J. Wang, F. Zhang and Q. An, *Energy Environ. Sci.*, 2021, **14**, 3945.
10. M. Nonnenmacher, M. P. O'Boyle and H. K. Wickramasinghe, *Appl. Phys. Lett.*, 1991, **58**, 2921.
11. M. Mingebach, C. Deibel and V. Dyakonov, *Phys. Rev. B*, 2011, **84**, 153201.
12. H. Feng, X. Song, Z. Zhang, R. Geng, J. Yu, L. Yang, D. Baran and W. Tang, *Adv. Funct. Mater.*, 2019, **29**, 1903269.
13. L. J. A. Koster, V. D. Mihailetchi, H. Xie and P. W. M. Blom, *Appl. Phys. Lett.*, 2005, **87**, 203502.
14. L. J. A. Koster, V. D. Mihailetchi, R. Ramaker and P. W. M. Blom, *Appl. Phys. Lett.*, 2005, **86**, 123509.
15. S. Ryu, N. Y. Ha, Y. H. Ahn, J.-Y. Park and S. Lee, *Sci. Rep.*, 2021, **11**, 16781.
16. K. A. Luck, V. K. Sangwan, P. E. Hartnett, H. N. Arnold, M. R. Wasielewski, T. J. Marks and M. C. Hersam, *Adv. Funct. Mater.*, 2017, **27**, 1703805.
17. I. Zonno, H. Zayani, M. Grzeslo, B. Krogmeier and T. Kirchartz, *Phys. Rev. Applied*, 2019, **11**, 054024.
18. F. Fabregat-Santiago, G. Garcia-Belmonte, I. Mora-Seró and J. Bisquert, *Phys. Chem. Chem. Phys.*, 2011, **13**, 9083.
19. S. Cho, K.-D. Kim, J. Heo, J. Y. Lee, G. Cha, B. Y. Seo, Y. D. Kim, Y. S. Kim, S.-Y. Choi and D. C. Lim, *Sci. Rep.*, 2014, **4**, 4306.
20. G. Jeong, J. Seo, Y. Kim, D.-H. Seo, J. M. Baik, E.-C. Jeon, G. Lee and H. Park, *ACS Appl. Mater. Interfaces*, 2021, **13**, 22000.
21. M. Rosa, S. Corni and R. Di Felice, *Phys. Rev. B*, 2014, **90**, 125448.
22. W. Liu, J. Carrasco, B. Santra, A. Michaelides, M. Scheffler and A. Tkatchenko, *Phys. Rev. B*, 2012, **86**, 245405.

23. C. G. Shuttle, R. Hamilton, J. Nelson, B. C. O'Regan and J. R. Durrant, *Adv. Funct. Mater.*, 2010, **20**, 698.
24. W. R. Mateker and M. D. McGehee, *Adv. Mater.*, 2017, **29**, 1603940.
25. J. Wang, H. Yu, C. Hou and J. Zhang, *ACS Appl. Mater. Interfaces*, 2020, **12**, 26543–26554.
26. H. Bin, J. Wang, J. Li, M. M. Wienk and R. A. J. Janssen, *Adv. Mater.*, 2021, **33**, 2008429.
27. H. Cheng, Y. Li, G. Zhao, K. Zhao and Z. S. Wang, *ACS Appl. Mater. Interfaces*, 2019, **11**, 28960.
28. A. Pockett, H. K. H. Lee, B. L. Coles, W. C. Tsoi and M. J. Carnie, *Nanoscale*, 2019, **11**, 10872.
29. E. von Hauff, *J. Phys. Chem. C*, 2019, **123**, 11329.
30. N. Gasparini, M. Salvador, S. Strohm, T. Heumueller, I. Levchuk, A. Wadsworth, J. H. Bannock, J. C. de Mello, H.-J. Egelhaaf, D. Baran, I. McCulloch and C. J. Brabec, *Adv. Energy Mater.*, 2017, **7**, 1700770.
31. J. Ho Kim, S.-N. Kwon, S.-in Na, S.-K. kim, Y.-Zo Yoo, H.-S. Im, and T.-Y. Seong, *J. Electron. Mater.*, 2017, **46**, 2140.
32. A. Li, R. Nie, X. Deng, H. Wei, S. Zheng, Y. Li, J. Tang and K.-Y. Wong, *Appl. Phys. Lett*., 2014, **104**, 123303.
33. W. Li, Y. Qin, W. Dai and D. Zhou, *J. Mater. Sci. Mater. Electron.*, 2018, **29**, 11296.
34. J. Wang, K. Fukuda, D. Inoue, D. Hashizume, L. Sun, S. Xiong, T. Yokota and T. Someya, *ACS Appl. Mater. Interfaces*, 2022, **14**, 14165.
35. J. S. Kim, J. H. Park and Ji H. Lee, *Appl. Phys. Lett.*, 2007, **91**, 112111.
36. W. Wu, P. Huang, Y. Gao, Ji Wan, R. Sun and J. Min, *Small*, 2025, **21**, 2406773.